



Deposited via The University of Leeds.

White Rose Research Online URL for this paper:

<https://eprints.whiterose.ac.uk/id/eprint/215106/>

Version: Accepted Version

Article:

Rogger, J., Judd, E.J., Mills, B.J.W. et al. (2024) Bio-geographic climate sensitivity controls Earth system response to Large Igneous Province carbon degassing. *Science*, 385 (6709). pp. 661-666. ISSN: 0036-8075

<https://doi.org/10.1126/science.adn3450>

This is the author's version of the work. It is posted here by permission of the AAAS for personal use, not for redistribution. The definitive version was published in *Science* on Vol 385, Issue 6709, 8 Aug 2024, DOI: 10.1126/science.adn3450.

Reuse

Items deposited in White Rose Research Online are protected by copyright, with all rights reserved unless indicated otherwise. They may be downloaded and/or printed for private study, or other acts as permitted by national copyright laws. The publisher or other rights holders may allow further reproduction and re-use of the full text version. This is indicated by the licence information on the White Rose Research Online record for the item.

Takedown

If you consider content in White Rose Research Online to be in breach of UK law, please notify us by emailing eprints@whiterose.ac.uk including the URL of the record and the reason for the withdrawal request.

31 Large Igneous Provinces (LIPs) represent major perturbations to the Earth system,
32 triggering environmental changes that can result in severe mass extinctions on land and in the
33 ocean (1, 2). Climate warming following the degassing of massive amounts of carbon in
34 geologically instantaneous time is considered one of the main triggers of LIP-associated biological
35 extinctions and reorganizations (1). The severity and duration of the climate perturbation depend
36 on how fast the emitted carbon is returned to Earth's interior by climate feedback mechanisms
37 such as silicate mineral weathering and organic carbon burial (3, 4). The efficiency of the carbon-
38 climate regulation system, however, may in turn be affected by terrestrial and marine ecosystems
39 being shifted to a state of disequilibrium and maladaptation (5–8).

40 The terrestrial vegetation plays an integral part in the long-term carbon-climate regulation
41 system, but its functioning is sensitive to abrupt environmental changes. Primary productivity
42 determines the extent of photosynthetic carbon assimilation and the burial of organic carbon as a
43 net CO₂ sink. Vegetation can further enhance CO₂ consumption through silicate mineral
44 weathering reactions, for example by releasing reactive species like organic acids and chelators
45 into the soil during nutrient acquisition, or by intensifying the local hydrological cycle and
46 prolonging water–mineral contact times (9–14). LIP-triggered environmental perturbations
47 modify vegetation structure and functioning, causing species extinctions, range shifts,
48 deforestation, reductions in organic carbon burial, and the spread of opportunistic species into
49 newly freed habitats until more adapted plant communities reestablish (5–7, 15–17). To what
50 extent and how fast vegetation functions recover from LIP-induced climatic changes depends on
51 the capacity of plants to disperse and follow suitable habitats in a given paleogeographic setting
52 (18) and to adjust to new conditions through evolutionary adaptation (19, 20). After the most
53 severe mass extinction in Earth's history around 252 Ma ago, triggered by the Siberian Traps LIP,
54 the recovery of vegetation diversity and productivity to pre-LIP levels required several million
55 years (7, 15, 16). During this recovery period, the efficiency of the carbon-climate regulation
56 system may have been reduced due to weakened vegetation–weathering interactions and reduced
57 primary productivity. The long-term climatic consequences of LIP degassing events may be
58 dictated not only by intrinsic characteristics of the LIP episode, such as the mass of emitted
59 greenhouse gases, but also by the biological response and bio-climatic interactions in a given
60 paleogeographic setting.

61 Here, we use an eco-evolutionary vegetation model and proxy-based temperature
62 reconstructions to investigate how the climate adaptation capacity of vegetation, by dispersal and
63 adaptive evolution, may have affected geologic carbon fluxes and the long-term climate evolution
64 after episodes of Phanerozoic LIP degassing. We consider three LIPs, the Siberian Traps
65 (Permian–Triassic boundary; \approx 252 Ma), the Central Atlantic Magmatic Province (Triassic–
66 Jurassic boundary; \approx 201 Ma) and the North Atlantic Igneous Province (Paleocene–Eocene

67 boundary; ≈ 56 Ma). The LIPs differed in the severity of the triggered biological and climatic
68 consequences and occurred under contrasting paleogeographic configurations. During the Siberian
69 Traps and the Central Atlantic Magmatic Province, most continental land mass was assembled in
70 the supercontinent Pangea. The two LIPs are assumed to have caused two of the most severe mass
71 extinctions in Earth's history (1). The Siberian Traps further resulted in a multi-million-year
72 hyperthermal of elevated atmospheric CO_2 and temperatures (21, 22). The North Atlantic Igneous
73 Province occurred under a more modern paleogeography with dispersed continents, and it caused
74 the most severe warming event during the Cenozoic (Paleocene-Eocene Thermal Maximum,
75 PETM) (23). While less severe in terms of species extinctions, it still induced a major
76 reorganization of biological systems on land and in the ocean (24).

77 The eco-evolutionary model is designed to capture major vegetation dynamics in response
78 to climate perturbations, including dispersal, adaptation and competition. It is coupled to models
79 of the geologic carbon cycle and climate. The climate trajectory after an imposed LIP degassing
80 episode depends on how fast the released carbon is returned from the atmosphere-ocean system to
81 geologic carbon reservoirs through silicate weathering and organic carbon burial. Silicate
82 weathering is modelled as a function of local erosion, runoff, temperature and vegetation-mediated
83 weathering enhancement. In areas of high plant productivity, a maximum four-fold or six-fold
84 (Supplementary Materials; SM) weathering enhancement is considered compared with
85 unvegetated land (9, 10, 12, 25). Marine organic carbon production and burial depend on local sea
86 surface temperatures and continental weathering as a nutrient source, while vegetation productivity
87 and terrestrially derived organic carbon burial depend on solar radiation, aridity, temperature and
88 the vegetation adaptation state. Primary productivity and weathering enhancement are calculated
89 by modelling vegetation units that populate the continents and that can disperse and adapt in
90 response to climatic changes at specified rates. The vegetation units represent plant assemblages,
91 which we term 'floras', and depict the ensemble response of their constituents. Floras are
92 characterized by a gaussian niche, defined by an optimum mean annual temperature (MAT) and
93 Budyko aridity index (BAI) at which their physiological potential is greatest. The climate niche
94 determines a geographic space in which a flora can be productive (niche range of 10°C in MAT
95 and 2 BAI units; see SM and fig. S1 for derivation). The LIP-triggered climate warming can cause
96 a discrepancy between a flora's optimum niche and the local environment, resulting in reduced
97 productivity and vegetation-mediated weathering enhancement, until a better adapted flora
98 disperses to the location, or the original flora adapts to the new conditions through adaptive
99 evolution. By testing a wide parameter range for rates of flora dispersal (varying the scale
100 parameter of the dispersal kernel between $0\text{--}100,000$ km Ma^{-1}) and niche evolution (speed of
101 temperature niche adaptation $0\text{--}10^\circ\text{C Ma}^{-1}$; aridity niche adaptation $0\text{--}100$ BAI units Ma^{-1}), we

102 explore the sensitivity of LIP-triggered climatic perturbations to the vegetation's adaptation
103 capacity in a given paleogeographic configuration.

104 **Vegetation recovery shapes long-term climate trajectory and steady state**

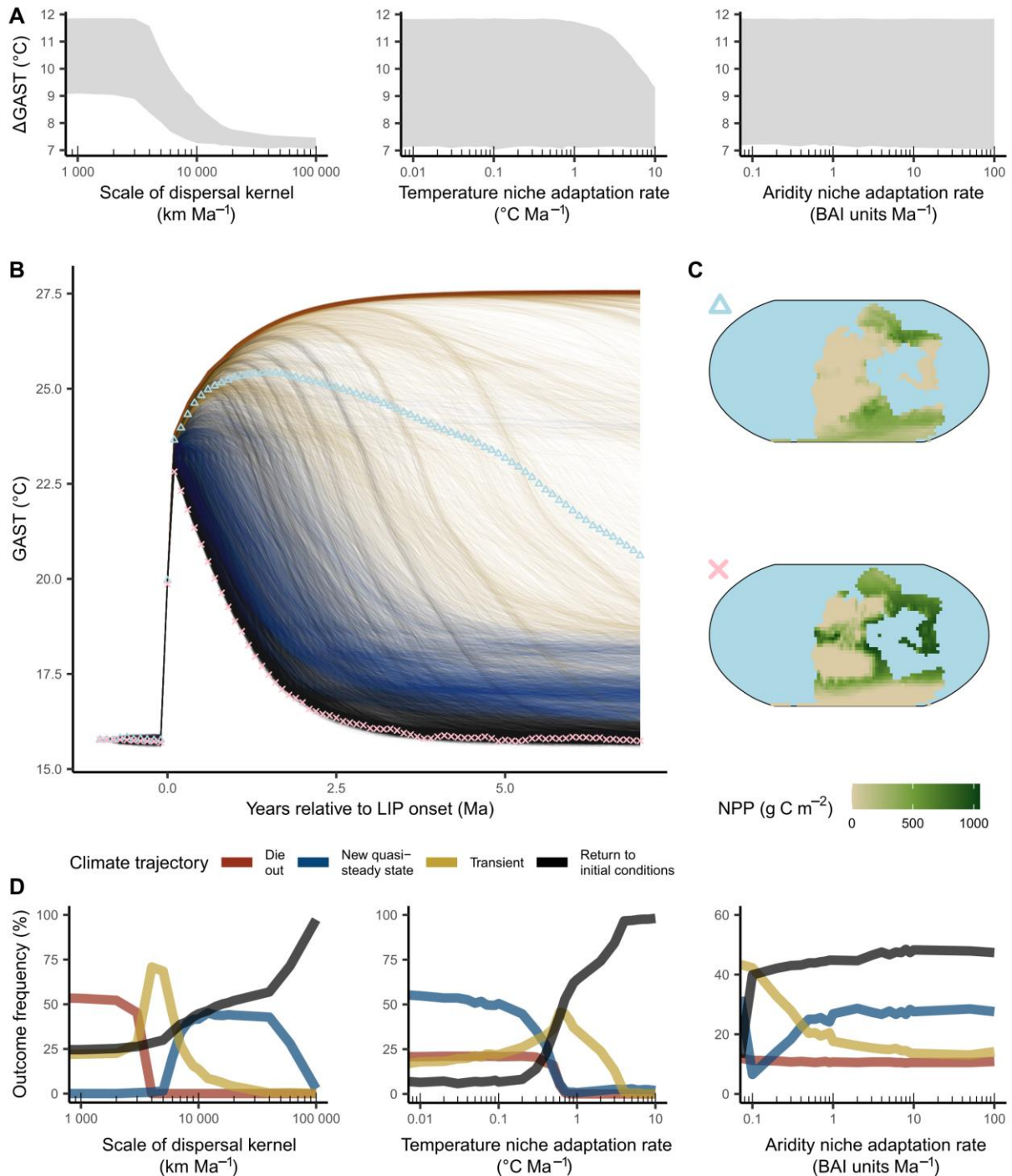
105 The vegetation's climate adaptation capacity and its effects on organic carbon burial and
106 silicate weathering rates affect the severity and duration of the temperature excursion, as well as
107 the long-term climatic steady state, after a LIP degassing event (fig. 1A). Using the
108 paleogeography of the Permian-Triassic mass extinction and a LIP degassing of 40,000 Gt of
109 carbon in 200 ka (3), modelled global average surface temperature (GAST) warming is between
110 7°C and 12°C, with greater warming in simulations in which floras have a limited capacity to
111 disperse in geographic space or to adapt their climatic niche to local environmental conditions by
112 adaptive evolution. The climate trajectories recovered from the simulations show four categories
113 of behavior (fig. 1B): the 'return', 'die out', 'new quasi-steady state', and 'transient' trajectories.
114 'Return' trajectories describe a full recovery of the GAST to temperatures similar to those before
115 the degassing event. This scenario is characterized by an ephemeral temperature excursion during
116 which carbon sinks temporarily fail to effectively remove carbon from the atmosphere-ocean
117 system. This is caused by a vegetation adaptation lag, resulting in reductions in vegetation-
118 mediated weathering enhancement and organic carbon burial. During the temperature excursion,
119 these processes can temporarily offset the effects of higher temperatures and a more active
120 hydrological cycle on silicate weathering. As the vegetation recovers, the strength of carbon
121 feedback mechanisms is re-established, and excess carbon is effectively removed from the
122 atmosphere-ocean system (complete set of carbon fluxes shown in fig. S2).

123 In a large proportion of the simulations, a 'new quasi-steady state' climate emerges,
124 characterized by stabilization of the GAST at a higher temperature than before the degassing event.
125 This scenario is characterized by carbon flux dynamics similar to those in the 'return' scenario,
126 with the exception that the vegetation does not fully recover from the climatic perturbation. As a
127 result, land-derived organic carbon burial and vegetation-mediated silicate weathering
128 enhancement stabilize at a lower level than before the degassing event, resulting in a higher GAST.
129 The new quasi-steady-state temperature is high enough that the direct climatic effects of
130 temperature and increased runoff on silicate weathering counterbalance the solid Earth carbon
131 degassing, despite the less adapted vegetation. A full vegetation recovery is prevented by the
132 presence of dispersal barriers (e.g., oceans, deserts and areas with better-adapted competitors) that
133 hinder floras in following their optimum climatic niche under a limited speed of *in situ*
134 evolutionary adaptation. The resulting climate state is considered a quasi-steady state, as continued
135 adaptive evolution, changes in degassing rates, or paleogeography beyond the considered model
136 duration would promote further climatic changes.

137 The 'transient' category includes climate trajectories that reached neither the initial nor a
138 new quasi-steady-state GAST within the modelled period but would presumably do so if a longer

139 time horizon was considered. Finally, 'die out' trajectories correspond to situations in which the
140 terrestrial vegetation is not able to cope with the climatic changes and possibly vanishes
141 completely. In this trajectory, temperatures continue to increase until silicate weathering can
142 compensate for the carbon degassing in the absence of vegetation.

143 The trajectory of a LIP-triggered carbon-climate excursion is determined by the
144 combination of the vegetation's dispersal and climate adaptation capacity (fig. 1D). 'Die out'
145 trajectories are limited to models assuming very low dispersal capacities. For temperature
146 adaptation speeds lower than $1^{\circ}\text{C Ma}^{-1}$, simulations predict an increased likelihood of reaching a
147 new climatic quasi-steady state. This is because the warming exceeds the *in situ* temperature
148 adaptation capacity, thus triggering a dispersal response and a redistribution of floras, which can
149 result in an incomplete recovery and less productive vegetation distribution. The aridity adaptation
150 capacity limits the geographic space into which a flora can disperse. Therefore, simulations predict
151 an increased proportion of transient trajectories with a slow climatic recovery in the low aridity
152 adaptation range. We observe a full recovery from the climate perturbation only in simulations
153 considering the highest dispersal and temperature adaptation rates, enabling floras to efficiently
154 track their climatic niche or eliminate the need for migration, respectively. Such dispersal and
155 temperature niche adaptation rates represent the upper end of what can be considered a plausible
156 range for plants (18–20, 26, 27). Considering more likely temperature niche adaptation rates of 0–
157 $3^{\circ}\text{C Ma}^{-1}$ (median below 1°C) (19, 26), non-zero aridity adaptation (19), and the exclusion of
158 unrealistic dispersal values that result in 'die out' trajectories, all three of the categories 'return',
159 'new quasi-steady state' and 'transient' are plausible climate trajectories following a LIP degassing
160 of the intensity estimated to have occurred at the Permian–Triassic boundary.



161
 162
 163 **Figure 1: Sensitivity of modelled post-Large Igneous Province (LIP) climate trajectories to eco-evolutionary**
 164 **vegetation dynamics.** **A.** Range of modelled global average surface temperature (GAST) increase depending on the
 165 terrestrial vegetation's adaptation capacity. The dispersal value represents the scale parameter of a Weibull distribution
 166 with shape parameter value of two, from which dispersal values of modelled floras are randomly drawn. A flora's
 167 aridity niche is characterized by a range of the Budyko aridity index (BAI). Aridity adaptation speed is thus expressed
 168 as BAI units per Ma. **B.** Range of climate trajectories observed for different vegetation adaptation capacities. Each
 169 line represents a separate model run with a different combination of vegetation dispersal and climatic niche adaptation
 170 capacity. 'Die out': model outcomes with less than 10^{12} mol C yr^{-1} terrestrial organic carbon burial at the end of the
 171 simulation and a high temperature steady state, 'return': complete recovery of climate from perturbation (Δ GAST
 between end and beginning of simulation $< 0.5^{\circ}\text{C}$), 'new quasi-steady state': stabilization at a higher global average

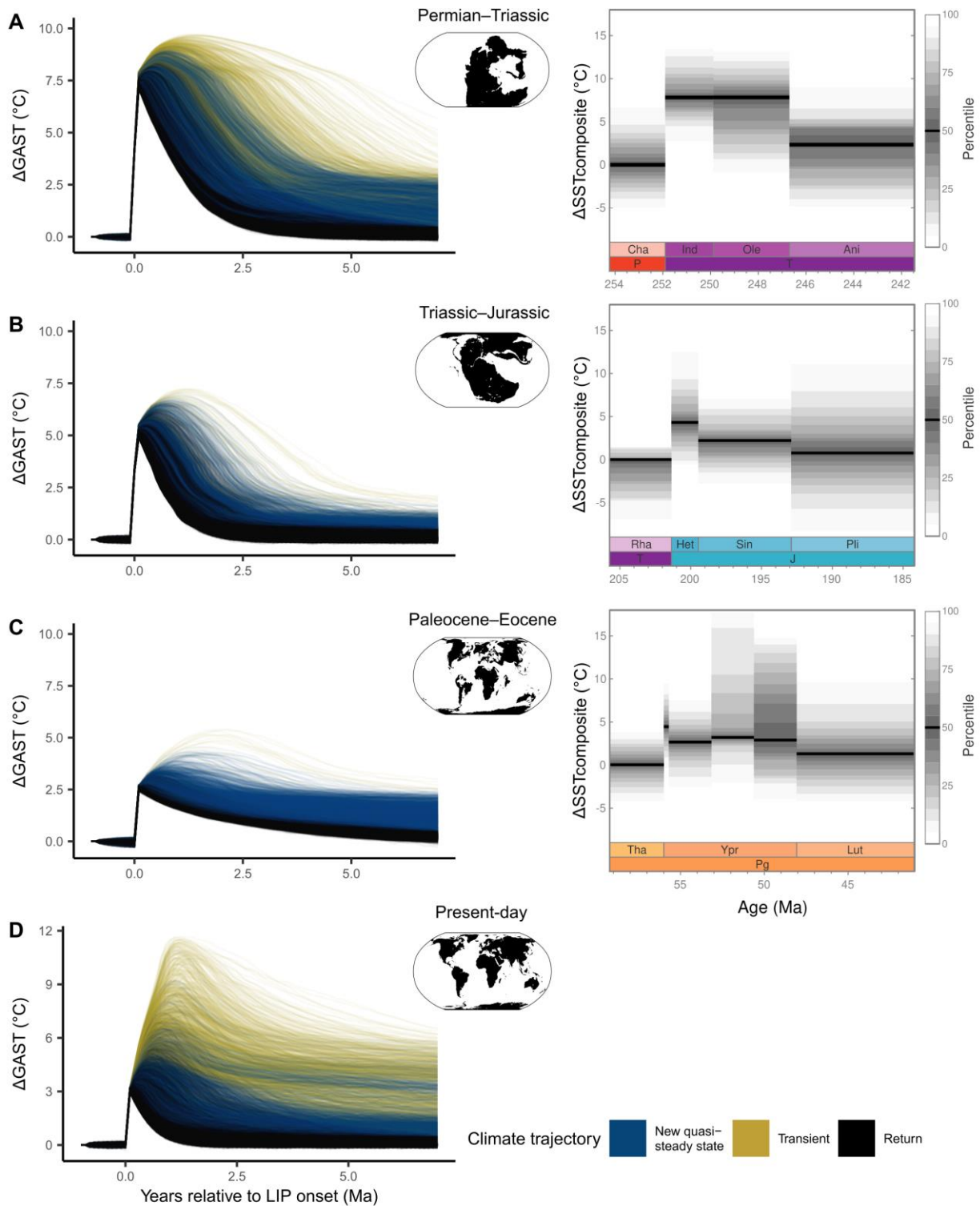
172 temperature (minimum of +0.5°C compared to initial conditions, $\Delta GAST < 0.5^\circ\text{C}$ and $\Delta F_{locb} < 5 \cdot 10^{10} \text{ mol C yr}^{-1}$
173 during the last two million model years), ‘transient’: none of the above occurs until the end of the simulation. All
174 carbon fluxes associated with the different climate trajectories are shown in fig. S2. **C.** Spatial net primary productivity
175 (NPP) plots showing the distribution of productivity for a ‘return’ (bottom) and a ‘transient’ (top) scenario 2 Ma after
176 the LIP onset. **D.** Model outcome frequency depending on biological adaptation parameters. In total, 12,122 parameter
177 combinations were tested (19 Weibull dispersal scale parameters, and 29 temperature- and 22 aridity-adaptation rates).

178 **Bio-climatic response to Phanerozoic LIPs**

179 Simulations produce climate trajectories that correspond well with the variable temperature
180 responses reconstructed for different Phanerozoic LIPs (fig. 2). We compiled multi-million-year
181 composite sea surface temperature reconstructions spanning the emplacement and aftermath of the
182 Siberian Traps, the Central Atlantic Igneous Province and the North Atlantic Igneous Province
183 LIPs based on several geochemical proxy systems and from different locations around the globe
184 (see SM). We applied the coupled vegetation–carbon-cycle model to the corresponding
185 paleogeographic settings and varied boundary conditions, i.e., pre-LIP atmospheric CO₂
186 concentration and mass and duration of the LIP carbon degassing, within estimated ranges [600
187 ppm, 40,000 Gt C, 200 ka, for the Siberian Traps (21, 28, 29), 800 ppm, 30,000 Gt C, 200 ka, for
188 the Central Atlantic Igneous Province (30, 31) and 500 ppm, 15,000 Gt C, 100 ka (step injection)
189 (32–34), for the North Atlantic Igneous Province, respectively; alternative scenarios in fig. S3]. In
190 doing so we identify eco-evolutionary vegetation dynamics as a possible cause of the variability
191 in post-LIP climate evolution – excluding models with unrealistic dispersal scales that would result
192 in ‘die-out’ trajectories and considering only models with non-zero temperature and aridity niche
193 adaptation rates.

194 Geologic proxies suggest the most severe and sustained warming for the Siberian Traps
195 (Permian-Triassic), with temperatures increasing by 5–10°C over 5 Ma following the LIP and a
196 subsequent recovery of temperatures to about 2.5°C higher than before the LIP. This severity and
197 multi-million-year warming, as well as a possible shift to a new climate quasi-steady state, is
198 reproduced in the model when a strongly impacted vegetation with a limited climate adaptation
199 capacity by dispersal and evolution is assumed, resulting in a sustained reduction of the efficiency
200 of the carbon–climate regulation system. The resulting reduction in the ratio of organic to total
201 carbon burial further results in an excursion of approximated carbonate $\delta^{13}\text{C}$ signatures, in
202 agreement with proxy records for the period (up to –6 ‰; fig. S4). Applying the same biological
203 parameter space to the Central Atlantic Igneous Province (Triassic-Jurassic), we simulate less
204 severe temperature excursions, with an initial warming of around 5°C and a relatively rapid and
205 continuous recovery of temperatures thereafter, in line with the proxy data. This suggests a faster
206 recovery of vegetation and carbon-cycle feedback mechanisms after the LIP perturbation, with the
207 excess carbon being captured effectively through silicate weathering and organic carbon burial.
208 For the North Atlantic Igneous Province, the proxy record reveals a short-lived initial warming of

209 3–5°C (the PETM), followed by a multi-million-year increase in temperatures of approximately
210 2.5°C (the Early Eocene Climatic Optimum). This is in agreement with a large range of possible
211 new climatic quasi-steady states modelled for the respective paleogeography. We further model a
212 hypothetical LIP of 10,000 Gt C to test the response for the present-day continental configuration,
213 assuming a starting CO₂ concentration of 400 ppm. Despite the lower mass of carbon injected, a
214 similar set of trajectories as for the Permian-Triassic is observed, ranging from rapid recovery to
215 very severe and sustained warming in models with a reduced biological adaptation capacity. This
216 tendency for severe warming is caused by a particularly strong reduction in the carbon burial
217 capacity following the LIP-triggered vegetation disturbance (fig. S5), and by the low initial CO₂
218 concentration that results in a sensitive temperature to CO₂ response (fig. S6), amplifying the
219 warming and vegetation disturbance.



220
221
222
223
224
225
226
227
228

Figure 2: Comparison of modelled and reconstructed temperature changes for different Phanerozoic Large Igneous Province (LIP) degassing events. Δ GAST represents the change in the modelled global average surface temperature. Δ SST_{composite} represents a composite temperature change reconstructed from several geologic proxy systems and sample locations around the globe, based on data compiled in the PhanSST database (53); see Supplementary Materials for the derivation of temperature values. **A.** Siberian Traps LIP (Permian–Triassic boundary), **B.** the Central Atlantic Magmatic Province (Triassic–Jurassic boundary) and **C.** the North Atlantic Igneous Province (Paleocene–Eocene boundary). **D.** Hypothetical LIP scenario for present-day geography. See the main text for pre-LIP starting CO₂ concentration, LIP C degassing mass and LIP duration. An alternative set of scenarios

229 regarding the magnitude and duration of degassing, as well as sensitivity to plant weathering enhancement, is explored
230 in fig. S3. Paleogeographies are taken from (54) and (55).

231 **Bio-geographic climate sensitivity**

232 Eco-evolutionary dynamics and climate evolution reveal strong interactions with the
233 paleogeographic setting and LIP characteristics. Each geography is characterized by a distinct set
234 of possible climate trajectories following a carbon injection (figs 2 & S3). Differences include the
235 tendency for severe and persistent hyperthermals (e.g., Permian-Triassic and present-day
236 configuration) or the chance to result in a warmer climatic quasi-steady state (e.g., Paleocene-
237 Eocene). Our results suggest that these differences are caused by interacting biotic and abiotic
238 factors. Abiotic and geographic factors include the magnitude of the LIP degassing event, the pre-
239 event climate state (i.e., radiative forcing), and the response of temperature and the hydrological
240 cycle to an increase in greenhouse gases (fig. S6). Together, these factors determine the severity
241 of the initial climatic and biological perturbation. The recovery from this perturbation, however,
242 is shaped by interacting biological and abiotic processes, as different geographic configurations
243 cause different local environmental changes and stresses to the vegetation, but also shape recovery
244 dynamics by determining possible migration routes. More fragmented continental configurations,
245 like during the Paleocene-Eocene compared to supercontinent configurations, enhance the
246 likelihood of a shift to a new climatic quasi-steady state, as dispersal barriers slow down biological
247 recovery. Differences in the abundance and disturbance of regions with high rates of weathering
248 and primary productivity tend to determine the efficiency of the post-LIP carbon regulation system
249 and the resulting climatic evolution (figs S5 & S7). The coupled biotic and abiotic response to a
250 perturbation can be considered a ‘bio-geographic’ climate sensitivity that is unique to every
251 paleogeographic configuration and biota present in a given period.

252 **Vegetation eco-evolution and the long-term carbon-climate system**

253 By combining simulations and proxy-based climate reconstructions, we show how the
254 evolution of the physical environment following a LIP-triggered perturbation is shaped by
255 biological vegetation dynamics. Eco-evolutionary processes, including dispersal, evolution and
256 competition, that determine the resilience and distribution of primary productivity and vegetation–
257 weathering interactions can interfere with the carbon-climate regulation system, resulting in a large
258 range of possible climate trajectories following a carbon cycle perturbation. The feedback
259 documented here represents an important addition to the regulation mechanisms previously
260 considered to shape the multi-million-year climate evolution following a massive carbon injection
261 to Earth’s atmosphere and oceans (3, 35–39).

262 LIP characteristics, paleogeography and eco-evolutionary vegetation dynamics combine to
263 shape the temperature trajectories observed in simulations and the data for selected Phanerozoic
264 LIPs. For the Permian–Triassic transition, we observe that the combination of the severe initial
265 warming caused by the Siberian Traps and a limited vegetation adaptation capacity reduces the
266 efficiency of the carbon regulation system and results in elevated atmospheric CO₂ and
267 temperatures for several millions of years after the perturbation. Our temperature reconstruction
268 and simulated scenarios are in agreement with other climatic reconstructions for the period (21,
269 22) and with the especially slow vegetation recovery observed in the fossil record in comparison
270 to other extinction events (7, 15, 40, 41). After the Permian-Triassic mass extinction, it may have
271 taken 4–5 Ma for stable forest ecosystems to re-establish (15, 42, 43). This could have played a
272 particularly large role in slowing down the climatic recovery, considering the importance of deep-
273 rooting trees in mediating plant–weathering interactions and carbon assimilation (13). In contrast,
274 the geologic record and simulations indicate a faster recovery of temperatures for the Triassic-
275 Jurassic hyperthermal, suggesting that the bio-geographic conditions permitted a faster
276 equilibration and recovery of vegetation and the carbon-climate system. Other abiotic and biotic
277 factors could have amplified differences in the vegetation response and climate evolution between
278 the considered LIPs. Short-term ‘kill mechanisms’ such as acid rain, aerosol-induced climatic
279 change, halogen toxicity, and increased levels of ultraviolet-B radiation could have reduced initial
280 vegetation fitness and the ability of vegetation to respond to long-term climate changes (1, 44, 45).
281 More severe climate warming is further modelled when floras are less adapted at the onset of the
282 LIP, for example due to a previous climatic perturbation (fig. S9). Distinct environmental
283 perturbations during the LIP emplacement result in different post-LIP plant community structures,
284 with differences in functioning and ecological stability beyond the generalized vegetation response
285 captured in the present model (40, 42, 43). Additional vegetation adaptation lags could be caused
286 by a limited dispersal success, which is affected not only by the distribution of climatic zones, but

287 also by the distribution and formation of appropriate soil conditions (42, 46) and the effect of
288 climatic changes on dispersal vectors (47). Our results emphasize the importance of considering
289 such LIP-triggered biological dynamics in shaping the Earth system response to severe warming.

290 The LIP-triggered vegetation response can cause a transition to a new climatic quasi-steady
291 state. Combined simulations and data indicate that a new equilibrium can be reached after a multi-
292 million-year high-temperature period (i.e., Permian-Triassic) or relatively rapidly after the initial
293 carbon cycle perturbation, as observed for the Paleocene–Eocene transition. In contrast to the
294 Siberian Traps, the floral recovery after the North Atlantic Igneous Province and the PETM is
295 assumed to have occurred rapidly through plant dispersal (48) and less severely impacted plant
296 communities (49). Our results indicate that, for variable speeds of the biological and climatic
297 recovery, a main effect of LIPs is to trigger a process of vegetation turnover and reorganization
298 that can change long-term rates of organic and inorganic carbon burial. These changes in carbon
299 fluxes result in a new carbon cycle balance at a different atmospheric CO₂ level than before the
300 perturbation (50, 51). Our findings are supported by limited climatic niche adaptation rates in
301 plants, which are considerably lower than the warming rates during these events (19, 20). Hence,
302 severe climate changes inevitably result in range shifts, competition and possibly the extinction of
303 specific floras, which permanently alter the distribution and intensity of vegetation-mediated
304 carbon fluxes. The vegetation reorganization may affect additional vegetation-climate interactions,
305 which can contribute to a shift in the climate state. These include changes in surface albedo,
306 affecting climate through an altered radiation balance [fig. S8; (52)], or changes in
307 evapotranspiration rates and water cycling, which may further amplify the influence of vegetation
308 shifts on weathering rates (fig. S3). Biological movement and vegetation dynamics are further
309 shaped by the paleogeographic configuration, which affects the speed of biotic recovery and
310 therefore the potential for long-term climatic shifts.

311 Throughout its history, Earth has experienced several severe mass extinctions and finds itself today
312 in another major bio-climatic crisis – this time not triggered by a LIP, but by anthropogenic
313 greenhouse gas emissions and land use. Our results show how the coupled response of biological
314 systems and the abiotic environment shape the long-term consequences of such perturbations and
315 reveal the possibility of a shift to a new climatic steady state.

References and Notes

- 317 1. D. P. Bond, P. B. Wignall, Large igneous provinces and mass extinctions: An update. *Volcanism,*
318 *Impacts, and Mass Extinctions: Causes and Effects* (Keller, G. and Kerr, A.C., eds.). *Geological*
319 *Society of America Special Paper 505*, DOI 10.1130/2014.2505(02) (2014).
- 320 2. M. J. Benton, Hyperthermal-driven mass extinctions: killing models during the Permian–Triassic
321 mass extinction. *Philosophical Transactions of the Royal Society A: Mathematical, Physical and*
322 *Engineering Sciences* **376**, 20170076, DOI 10.1098/rsta.2017.0076 (2018).
- 323 3. L. R. Kump, Prolonged Late Permian–Early Triassic hyperthermal: failure of climate regulation?
324 *Philosophical Transactions of the Royal Society A: Mathematical, Physical and Engineering*
325 *Sciences* **376**, 20170078, DOI 10.1098/rsta.2017.0078 (2018).
- 326 4. M. T. Jones, D. A. Jerram, H. H. Svensen, C. Grove, The effects of large igneous provinces on the
327 global carbon and sulphur cycles. *Palaeogeography, Palaeoclimatology, Palaeoecology* **441**, 4–
328 21, DOI 10.1016/j.palaeo.2015.06.042 (2016).
- 329 5. J. L. Payne *et al.*, Large Perturbations of the Carbon Cycle During Recovery from the End-Permian
330 Extinction. *Science* **305**, 506–509, DOI 10.1126/science.1097023 (2004).
- 331 6. Z.-Q. Chen, M. J. Benton, The timing and pattern of biotic recovery following the end-Permian
332 mass extinction. *Nature Geoscience* **5**, 375–383, DOI 10.1038/ngeo1475 (2012).
- 333 7. Z. Xu *et al.*, End Permian to Middle Triassic plant species richness and abundance patterns in
334 South China: Coevolution of plants and the environment through the Permian–Triassic transition.
335 *Earth-Science Reviews* **232**, 104136, DOI 10.1016/j.earscirev.2022.104136 (2022).
- 336 8. P. Hull, Life in the Aftermath of Mass Extinctions. *Current Biology* **25**, R941–R952, DOI 10.
337 1016/j.cub.2015.08.053 (2015).
- 338 9. L. L. Taylor *et al.*, Biological weathering and the long-term carbon cycle: integrating mycorrhizal
339 evolution and function into the current paradigm. *Geobiology* **7**, 171–191, DOI 10.1111/j.1472-
340 4669.2009.00194.x (2009).
- 341 10. K. L. Moulton, Solute flux and mineral mass balance approaches to the quantification of plant
342 effects on silicate weathering. *American Journal of Science* **300**, 539–570, DOI 10.2475/ajs.
343 300.7.539 (2000).
- 344 11. J. Quirk, M. Y. Andrews, J. R. Leake, S. A. Banwart, D. J. Beerling, Ectomycorrhizal fungi and
345 past high CO₂ atmospheres enhance mineral weathering through increased below-ground carbon-
346 energy fluxes. *Biology Letters* **10**, 20140375, DOI 10.1098/rsbl.2014.0375 (2014).
- 347 12. E. Berner, R. Berner, K. Moulton, Plants and Mineral Weathering: Present and Past. *Treatise on*
348 *Geochemistry* **5**, 169–188, DOI 10.1016/B0-08-043751-6/05175-6 (2003).
- 349 13. J. Quirk *et al.*, Constraining the role of early land plants in Palaeozoic weathering and global
350 cooling. *Proceedings of the Royal Society B: Biological Sciences* **282**, 20151115, DOI
351 10.1098/rspb.2015.1115 (2015).
- 352 14. T. M. Lenton, M. Crouch, M. Johnson, N. Pires, L. Dolan, First plants cooled the Ordovician.
353 *Nature Geoscience* **5**, 86–89, DOI 10.1038/ngeo1390 (2012).
- 354 15. L. Grauvogel-Stamm, S. R. Ash, Recovery of the Triassic land flora from the end-Permian life
355 crisis. *Comptes Rendus Palevol* **4**, 593–608, DOI 10.1016/j.crpv.2005.07.002 (2005).

- 356 16. G. J. Retallack, J. J. Veevers, R. Morante, Global coal gap between Permian–Triassic extinction
357 and Middle Triassic recovery of peat-forming plants. *Geological Society of America Bulletin* **108**,
358 195–207, DOI 10.1130/0016-7606(1996)108<0195:GCGBPT>2.3.CO;2 (1999).
- 359 17. P. McAllister Rees, Land-plant diversity and the end-Permian mass extinction. *Geology* **30**, 827,
360 DOI 10.1130/0091-7613(2002)030<0827:LPDATE>2.0.CO;2 (2002).
- 361 18. R. T. Corlett, D. A. Westcott, Will plant movements keep up with climate change? *Trends in*
362 *Ecology & Evolution* **28**, 482–488, DOI 10.1016/j.tree.2013.04.003 (2013).
- 363 19. H. Liu, Q. Ye, J. J. Wiens, Climatic-niche evolution follows similar rules in plants and animals.
364 *Nature Ecology & Evolution* **4**, 753–763, DOI 10.1038/s41559-020-1158-x (2020).
- 365 20. J. M. Bennett *et al.*, The evolution of critical thermal limits of life on Earth. *Nature*
366 *Communications* **12**, 1198, DOI 10.1038/s41467-021-21263-8 (2021).
- 367 21. M. M. Joachimski *et al.*, Five million years of high atmospheric CO₂ in the aftermath of the
368 Permian-Triassic mass extinction. *Geology* **50**, 650–654, DOI 10.1130/G49714.1 (2022).
- 369 22. Y. Sun *et al.*, Lethally Hot Temperatures During the Early Triassic Greenhouse. *Science* **338**, 366–
370 370, DOI 10.1126/science.1224126 (2012).
- 371 23. S. M. Jones, M. Hoggett, S. E. Greene, T. Dunkley Jones, Large Igneous Province thermogenic
372 greenhouse gas flux could have initiated Paleocene-Eocene Thermal Maximum climate change.
373 *Nature Communications* **10**, 5547, DOI 10.1038/s41467-019-12957-1 (2019).
- 374 24. F. A. McInerney, S. L. Wing, The Paleocene-Eocene Thermal Maximum: A Perturbation of
375 Carbon Cycle, Climate, and Biosphere with Implications for the Future. *Annual Review of Earth*
376 *and Planetary Sciences* **39**, 489–516, DOI 10.1146/annurev-earth-040610-133431 (2011).
- 377 25. T. M. Lenton, S. J. Daines, B. J. Mills, COPSE reloaded: An improved model of biogeochemical
378 cycling over Phanerozoic time. *Earth-Science Reviews* **178**, 1–28, DOI 10.1016/j.
379 earscirev.2017.12.004 (2018).
- 380 26. T. Jezkova, J. J. Wiens, Rates of change in climatic niches in plant and animal populations are
381 much slower than projected climate change. *Proceedings of the Royal Society B: Biological*
382 *Sciences* **283**, 20162104, DOI 10.1098/rspb.2016.2104 (2016).
- 383 27. Z. Lososová *et al.*, Seed dispersal distance classes and dispersal modes for the European flora.
384 *Global Ecology and Biogeography* **32**, 1485–1494, DOI 10.1111/geb.13712 (2023).
- 385 28. S. V. Sobolev *et al.*, Linking mantle plumes, large igneous provinces and environmental
386 catastrophes. *Nature* **477**, 312–316, DOI 10.1038/nature10385 (2011).
- 387 29. H. Svensen *et al.*, Siberian gas venting and the end-Permian environmental crisis. *Earth and*
388 *Planetary Science Letters* **277**, 490–500, DOI 10.1016/j.epsl.2008.11.015 (2009).
- 389 30. M. Capriolo *et al.*, Deep CO₂ in the end-Triassic Central Atlantic Magmatic Province. *Nature*
390 *Communications* **11**, 1670, DOI 10.1038/s41467-020-15325-6 (2020).
- 391 31. M. Steinthorsdottir, A. J. Jeram, J. C. McElwain, Extremely elevated CO₂ concentrations at the
392 Triassic/Jurassic boundary. *Palaeogeography, Palaeoclimatology, Palaeoecology* **308**, 418–432,
393 DOI 10.1016/j.palaeo.2011.05.050 (2011).
- 394 32. C. J. Hollis *et al.*, The DeepMIP contribution to PMIP4: methodologies for selection, compilation
395 and analysis of latest Paleocene and early Eocene climate proxy data, incorporating version 0.1 of

- 396 the DeepMIP database. *Geoscientific Model Development* **12**, 3149–3206, DOI 10.5194/gmd12-
397 3149-2019 (2019).
- 398 33. M. Gutjahr *et al.*, Very large release of mostly volcanic carbon during the Palaeocene–Eocene
399 Thermal Maximum. *Nature* **548**, 573–577, DOI 10.1038/nature23646 (2017).
- 400 34. M. Storey, R. A. Duncan, C. C. Swisher, Paleocene-Eocene Thermal Maximum and the Opening
401 of the Northeast Atlantic. *Science* **316**, 587–589, DOI 10.1126/science.1135274 (2007).
- 402 35. T. S. Tobin, C. M. Bitz, D. Archer, Modeling climatic effects of carbon dioxide emissions from
403 Deccan Traps volcanic eruptions around the Cretaceous–Paleogene boundary. *Palaeogeography,*
404 *Palaeoclimatology, Palaeoecology* **478**, 139–148, DOI 10.1016/j.palaeo.2016.05.028 (2017).
- 405 36. R. A. Berner, Examination of hypotheses for the Permo–Triassic boundary extinction by carbon
406 cycle modeling. *Proceedings of the National Academy of Sciences* **99**, 4172–4177, DOI
407 10.1073/pnas.032095199 (2002).
- 408 37. A. Grard, L. Francois, C. Dessert, B. Dupre, Y. Godderis, Basaltic volcanism and mass extinction
409 at the Permo-Triassic boundary: Environmental impact and modeling of the global carbon cycle.
410 *Earth and Planetary Science Letters* **234**, 207–221, DOI 10.1016/j.epsl.2005.02.027 (2005).
- 411 38. Y. Cui, L. R. Kump, Global warming and the end-Permian extinction event: Proxy and modeling
412 perspectives. *Earth-Science Reviews* **149**, 5–22, DOI 10.1016/j.earscirev.2014.04.007 (2015).
- 413 39. M. Capriolo *et al.*, Anthropogenic-scale CO₂ degassing from the Central Atlantic Magmatic
414 Province as a driver of the end-Triassic mass extinction. *Global and Planetary Change* **209**,
415 103731, DOI 10.1016/j.gloplacha.2021.103731 (2022).
- 416 40. J. C. McElwain, S. W. Punyasena, Mass extinction events and the plant fossil record. *Trends in*
417 *Ecology & Evolution* **22**, 548–557, DOI 10.1016/j.tree.2007.09.003 (2007).
- 418 41. D. H. Erwin, Lessons from the past: Biotic recoveries from mass extinctions. *Proceedings of the*
419 *National Academy of Sciences* **98**, 5399–5403, DOI 10.1073/pnas.091092698 (2001).
- 420 42. C. V. Looy, W. A. Brugman, D. L. Dilcher, H. Visscher, The delayed resurgence of equatorial
421 forests after the Permian–Triassic ecologic crisis. *Proceedings of the National Academy of*
422 *Sciences* **96**, 13857–13862, DOI 10.1073/pnas.96.24.13857 (1999).
- 423 43. C. V. Looy, R. J. Twitchett, D. L. Dilcher, J. H. A. Van Konijnenburg-Van Cittert, H. Visscher,
424 Life in the end-Permian dead zone. *Proceedings of the National Academy of Sciences* **98**, 7879–
425 7883, DOI 10.1073/pnas.131218098 (2001).
- 426 44. B. A. Black, L. T. Elkins-Tanton, M. C. Rowe, I. U. Peate, Magnitude and consequences of volatile
427 release from the Siberian Traps. *Earth and Planetary Science Letters* **317–318**, 363–373, DOI
428 10.1016/j.epsl.2011.12.001 (2012).
- 429 45. B. A. Black *et al.*, Systemic swings in end-Permian climate from Siberian Traps carbon and sulfur
430 outgassing. *Nature Geoscience* **11**, 949–954, DOI 10.1038/s41561-018-0261-y (2018).
- 431 46. M. A. Sephton, C. V. Looy, H. Brinkhuis, P. B. Wignall, J. W. De Leeuw, H. Visscher,
432 Catastrophic soil erosion during the end-Permian biotic crisis. *Geology* **33**, 941, DOI
433 10.1130/G21784.1 (2005).

- 434 47. J. C. McElwain, M. E. Popa, S. P. Hesselbo, M. Haworth, F. Surlyk, Macroecological responses
435 of terrestrial vegetation to climatic and atmospheric change across the Triassic/Jurassic boundary
436 in East Greenland. *Paleobiology* **33**, 547–573, DOI 10.1666/06026.1 (2007).
- 437 48. S. L. Wing *et al.*, Transient Floral Change and Rapid Global Warming at the Paleocene-Eocene
438 Boundary. *Science* **310**, 993–996, DOI 10.1126/science.1116913 (2005).
- 439 49. C. Jaramillo *et al.*, Effects of Rapid Global Warming at the Paleocene-Eocene Boundary on
440 Neotropical Vegetation. *Science* **330**, 957–961, DOI 10.1126/science.1193833 (2010).
- 441 50. M. P. D’Antonio, D. E. Ibarra, C. K. Boyce, Land plant evolution decreased, rather than increased,
442 weathering rates. *Geology* **48**, 29–33, DOI 10.1130/G46776.1 (2020).
- 443 51. B. J. W. Mills, S. Tennenbaum, D. Schwartzman, Exploring multiple steady states in Earth’s
444 longterm carbon cycle. *American Journal of Science* **321**, 1033–1044, DOI 10.2475/07.2021.01
445 (2021).
- 446 52. Y. Donnadieu, Y. Godderis, N. Bouttes, Exploring the climatic impact of the continental
447 vegetation on the Mesozoic atmospheric CO₂ and climate history. *Clim. Past* **5**, 85–96, DOI
448 10.5194/cp-5-85-2009 (2009).
- 449 53. E. J. Judd *et al.*, The PhanSST global database of Phanerozoic sea surface temperature proxy data.
450 *Scientific Data* **9**, 753, DOI 10.1038/s41597-022-01826-0 (2022).
- 451 54. C. Scotese, N. Wright, PALEOMAP Paleodigital Elevation Models (PaleoDEMS) for the
452 Phanerozoic. Available from: [https://www.earthbyte.org/paleodem-resource-scotese-and-wright-](https://www.earthbyte.org/paleodem-resource-scotese-and-wright-2018)
453 2018 (2018).
- 454 55. E. O. Straume, C. Gaina, K.H. Nisancioglu, Global Cenozoic Paleobathymetry with a focus on the
455 Northern Hemisphere Oceanic Gateways. *Gondwana Research* **86**, 126–143, DOI
456 10.1016/j.gr.2020.05.011 (2020).
- 457 56. E. J. Judd *et al.*, Data for: PhanSST - A global database of Phanerozoic sea surface temperature
458 proxy data, v0.0.1-beta, Zenodo (2022); <https://doi.org/10.5281/zenodo.7275402>.
- 459 57. J. Rogger *et al.*, Data and code for: Bio-geographic climate sensitivity controls Earth system
460 response to Large Igneous Province carbon degassing, Zenodo (2024);
461 <https://doi.org/10.5281/zenodo.12187757>.
- 462 58. O. Hagen *et al.*, gen3sis: A general engine for eco-evolutionary simulations of the processes that
463 shape Earth’s biodiversity. *PLOS Biology* **19**, e3001340, DOI 10.1371/journal.pbio.3001340
464 (2021).
- 465 59. M. Huang *et al.*, Air temperature optima of vegetation productivity across global biomes. *Nature*
466 *Ecology & Evolution* **3**, 772–779, DOI 10.1038/s41559-019-0838-x (2019).
- 467 60. M. J. Donoghue, E. J. Edwards, Biome shifts and niche evolution in plants. *Annual Review of*
468 *Ecology, Evolution, and Systematics* **45**, 547–572, DOI 10.1146/annurev-ecolsys-120213091905
469 (2014).
- 470 61. H. E. Beck *et al.*, Present and future Koppen-Geiger climate classification maps at 1-km resolution.
471 *Scientific Data* **5**, 180214, DOI 10.1038/sdata.2018.214 (2018).

- 472 62. A. Takeshima *et al.*, Global aridity changes due to differences in surface energy and water balance
473 between 1.5°C and 2°C warming. *Environmental Research Letters* **15**, 0940a7, DOI 10.1088/
474 1748-9326/ab9db3 (2020).
- 475 63. J. M. J. Travis *et al.*, Modelling dispersal: an eco-evolutionary framework incorporating
476 emigration, movement, settlement behaviour and the multiple costs involved. *Methods in Ecology*
477 *and Evolution* **3**, 628–641, DOI 10.1111/j.2041-210X.2012.00193.x (2012).
- 478 64. W. Cramer *et al.*, Comparing global models of terrestrial net primary productivity (NPP): overview
479 and key results. *Global Change Biology* **5**, 1–15, DOI 10.1046/j.1365-2486.1999.00009.x (1999).
- 480 65. M. J. Behrenfeld, P. G. Falkowski, Photosynthetic rates derived from satellite-based chlorophyll
481 concentration. *Limnology and Oceanography* **42**, 1–20, DOI 10.4319/lo.1997.42.1.0001 (1997).
- 482 66. B. J. Mills, Y. Donnadieu, Y. Godderis, Spatial continuous integration of Phanerozoic global
483 biogeochemistry and climate. *Gondwana Research* **100**, 73–86, DOI 10.1016/j.gr.2021.02.011
484 (2021).
- 485 67. A. J. West, Thickness of the chemical weathering zone and implications for erosional and climatic
486 drivers of weathering and for carbon-cycle feedbacks. *Geology* **40**, 811–814, DOI
487 10.1130/G33041.1 (2012).
- 488 68. P. Maffre *et al.*, Mountain ranges, climate and weathering. Do orogens strengthen or weaken the
489 silicate weathering carbon sink? *Earth and Planetary Science Letters* **493**, 174–185, DOI
490 10.1016/j.epsl.2018.04.034 (2018).
- 491 69. R. A. Berner, K. Caldeira, The need for mass balance and feedback in the geochemical carbon
492 cycle. *Geology* **25**, 955–956, DOI 10.1130/0091-7613(1997)025<0955:TNFMBA>2.3.CO;2
493 (1997).
- 494 70. J. K. Caves, A. B. Jost, K. V. Lau, K. Maher, Cenozoic carbon cycle imbalances and a variable
495 weathering feedback. *Earth and Planetary Science Letters* **450**, 152–163, DOI 10.1016/j.
496 epsl.2016.06.035 (2016).
- 497 71. G. A. Shields, B. J. W. Mills, Tectonic controls on the long-term carbon isotope mass balance.
498 *Proceedings of the National Academy of Sciences of the United States of America* **114**, 4318–
499 43232, DOI 10.1073/pnas.1614506114 (2017).
- 500 72. R. Berner, A model for atmospheric CO₂ over Phanerozoic time. *American Journal of Science*
501 **291**, 339–376, DOI 10.2475/ajs.291.4.339 (1991).
- 502 73. L. R. Kump, M. A. Arthur, Interpreting carbon-isotope excursions: carbonates and organic matter.
503 *Chemical Geology* **161**, 181–198, DOI 10.1016/S0009-2541(99)00086-8 (1999).
- 504 74. Y. Donnadieu *et al.*, A GEOCLIM simulation of climatic and biogeochemical consequences of
505 Pangea breakup. *Geochemistry, Geophysics, Geosystems* **7**, Q11019, DOI
506 10.1029/2006GC001278 (2006).
- 507 75. K. Fraedrich, A suite of user-friendly global climate models: Hysteresis experiments. *The*
508 *European Physical Journal Plus* **127**, 53, DOI 10.1140/epjp/i2012-12053-7 (2012).
- 509 76. O. Mehling, K. Bellomo, M. Angeloni, C. Pasquero, J. Von Hardenberg, High-latitude
510 precipitation as a driver of multicentennial variability of the AMOC in a climate model of

- 511 intermediate complexity. *Climate Dynamics* **61**, 1519–1534, DOI 10.1007/s00382-022-06640-3
512 (2023).
- 513 77. D. O. Gough, Solar interior structure and luminosity variations. *Solar Physics* **74**, 21–34 (1981).
- 514 78. E. Pucéat *et al.*, Revised phosphate–water fractionation equation reassessing paleotemperatures
515 derived from biogenic apatite. *Earth and Planetary Science Letters* **298**, 135–142, DOI 10.1016/
516 j.epsl.2010.07.034 (2010).
- 517 79. S.-T. Kim, J. R. O’Neil, Equilibrium and nonequilibrium oxygen isotope effects in synthetic
518 carbonates. *Geochimica et Cosmochimica Acta* **61**, 3461–3475, DOI 10.1016/S0016-
519 7037(97)00169-5 (1997).
- 520 80. M. Daëron *et al.*, Most Earth-surface calcites precipitate out of isotopic equilibrium. *Nature*
521 *Communications* **10**, 429, DOI 10.1038/s41467-019-08336-5 (2019).
- 522 81. L. Grossman, T.-L. Ku, Oxygen and carbon isotope fractionation in biogenic aragonite:
523 temperature effects. *Chemical Geology* **59**, 59–74 (1986).
- 524 82. S. B. Malevich, L. Vetter, J. E. Tierney, Global core top calibration of ¹⁸O in planktic foraminifera
525 to sea surface temperature. *Paleoceanography and Paleoclimatology* **34**, 1292–1315, DOI
526 10.1029/2019PA003576 (2019).
- 527 83. J. E. Tierney, M. P. Tingley, A Bayesian, spatially-varying calibration model for the TEX₈₆ proxy.
528 *Geochimica et Cosmochimica Acta* **127**, 83–106, DOI 10.1016/j.gca.2013.11.026 (2014).
- 529 84. J. E. Tierney, S. B. Malevich, W. Gray, L. Vetter, K. Thirumalai, Bayesian calibration of the
530 Mg/Ca paleothermometer in planktic foraminifera. *Paleoceanography and Paleoclimatology* **34**,
531 2005–2030, DOI 10.1029/2019PA003744 (2019).
- 532 85. M. Schobben *et al.*, Latest Permian carbonate carbon isotope variability traces heterogeneous
533 organic carbon accumulation and authigenic carbonate formation. *Climate of the Past* **13**, 1635–
534 1659, DOI 10.5194/cp-13-1635-2017 (2017).
- 535 86. T. Westerhold *et al.*, Astronomical calibration of the Ypresian timescale: implications for seafloor
536 spreading rates and the chaotic behavior of the solar system? *Climate of the Past* **13**, 1129–1152,
537 DOI 10.5194/cp-13-1129-2017 (2017).
- 538 87. T. Westerhold, U. Rohl, B. Donner, J. C. Zachos, Global extent of early Eocene hyperthermal
539 events: A new Pacific benthic foraminiferal isotope record from Shatsky Rise (ODP Site 1209).
540 *Paleoceanography and Paleoclimatology* **33**, 626–642, DOI 10.1029/2017PA003306 (2018).

541 **Acknowledgments:** All model simulations were conducted on the ETH Zurich computer cluster
542 ‘Euler’. The authors thank Melissa Dawes for English editing.

543 **Funding:** This work was supported by the Swiss National Science Foundation grant 192296
544 (to JR, TVG, and LP) and the UK Research and Innovation projects EP/Y008790/1 and
545 NE/X011208/1 (to BJWM).

546 **Author contributions:**

547 Conceptualization: JR, EJJ, BJWM, YG, TVG, LP

548 Software: JR

549 Formal Analysis: JR, EJJ

550 Supervision: TVG, LP

551 Validation: JR, EJJ, BJWM, YG, TVG, LP

552 Investigation: JR, EJJ

553 Visualization: JR, EJJ

554 Methodology: JR, EJJ, BJWM, YG, TVG, LP

555 Writing - original draft: JR, EJJ, BJWM, YG, TVG, LP

556 Writing review & editing: JR, EJJ, BJWM, YG, TVG, LP

557 Funding acquisition: TVG, LP

558 **Competing interests:** Authors declare that they have no competing interests.

559 **Data and materials availability:** All data sources are available in the manuscript or the
560 Supplementary Material. Proxy data for the paleotemperature estimations are available at Zenodo
561 (56), with further details described in (53). Model and analysis code are available at Zenodo (57).

562 **Supplementary Materials**

563 Materials and Methods

564 Figs. S1 to S13

565 References (58-87)

566

567

568

569

570

571

572

573

574

575

576

577

578

579

580

581

582

583

Supplementary Materials for

Bio-geographic climate sensitivity controls Earth system response to Large Igneous Province carbon degassing

Julian Rogger, Emily J. Judd, Benjamin J.W. Mills, Yves Godd ris, Taras V. Gerya, Lo c Pellissier

Corresponding author: julian.rogger@erdw.ethz.ch

The PDF file includes:

Materials and Methods

Figs. S1 to S13

References (58-87)

584 **Materials and Methods**

585 Model description

586 The model consists of three coupled components: an eco-evolutionary vegetation model, a
587 geologic carbon cycle model, and a look-up structure of pre-run climate model simulations.
588 Each presented climate trajectory represents a model run covering a time span of 8 Ma in time
589 steps of 100 ka and at a spatial resolution of $3.75^\circ \times 3.75^\circ$.

590 **Eco-evolutionary deep-time vegetation model.** The eco-evolutionary vegetation model tracks
591 vegetation primary productivity and vegetation-mediated enhancement of mineral weathering
592 as a function of a flora's productivity and state of adaptation to the local environmental
593 conditions. The developed vegetation model is based on *gen3sis* (58) (general engine for eco-
594 evolutionary simulations), a framework designed to model various biological entities and their
595 traits in a dynamic landscape, considering key processes such as dispersal, trait evolution and
596 competition. In the present model configuration, a biological entity represents a terrestrial
597 vegetation flora (assemblage of plants and symbiotic organisms living in a certain location at a
598 certain point in time) that is characterized by two key characteristics also observed for present-
599 day floras (59, 60): a temperature niche and an aridity niche (niche for water availability). In
600 the model, both characteristics are represented as a bell-shaped performance function around an
601 optimum (T_{opt} for temperature and A_{opt} for aridity) for each model flora. T_{opt} and A_{opt} need to
602 be understood as an ensemble response of all the organisms constituting a flora. The widths of
603 the temperature and aridity niches are derived from bio-climatic classification systems that are
604 often used to distinguish geographic regions with specific vegetation types (61). For the
605 temperature niche, the width approximates the variation in mean annual temperatures observed
606 within Koeppen-Geiger bio-climatic zones (approximately 10°C ; fig. S1). For aridity, the niche
607 width is approximated by the bin width of the Budyko aridity index (BAI) used to describe
608 different hydroclimatic regions on the globe [BAI for humid: 0–1.2, semi-humid: 1.2–2, semi-
609 arid: 2–4, arid: 4–6 (62); niche width of 2 BAI units used]. The *BAI* is defined as:

$$BAI = \frac{R_n}{\lambda \cdot P} \quad (1)$$

610 where R_n is the net surface radiation, λ the latent heat of vaporization, and P the precipitation.
611 Together, the temperature and aridity niche represent a geographic region in which a model
612 flora can be productive. If the climate changes to conditions a flora is not adapted to, it is forced
613 to adapt through migration and/or adaptive evolution of its niche.

614 The model is initialized with each terrestrial grid cell being occupied by an optimally adapted
615 flora, with T_{opt} and A_{opt} corresponding to the local temperature and aridity, respectively (the
616 possibility of a non-optimal adaptation state at the onset of the LIP is illustrated in fig. S9). At

617 each time step, floras can disperse to other terrestrial grid cells within a dispersal range that is
 618 newly drawn for each flora and at each time step from a right-skewed dispersal kernel defined
 619 by a Weibull distribution with shape parameter two and a varying scale parameter γ . The choice
 620 of the dispersal kernel accounts for the highly stochastic nature of dispersal (e.g., depending on
 621 vegetation characteristics, dispersal vectors or environmental conditions) as well as the
 622 generally high frequency of short-distance dispersal and low frequency of long-distance
 623 dispersal (18). By additionally scaling the dispersal distances according to the rate of a flora's
 624 primary productivity potential (NPP_{norm} , see eq. 11), we account for the various costs
 625 associated with the process of reproduction and dispersal, giving higher chances for long-
 626 distance dispersal to well adapted and productive floras (63). In the presented parameter
 627 exploration (e.g., figs 1 & 2), we vary the scale parameter γ of the dispersal kernel within a
 628 range of 0–100'000 km Ma⁻¹ (a multiple of Earth's circumference; considered unlimited
 629 dispersal) across the different simulations, covering a large range of empirically estimated plant
 630 dispersal abilities (unassisted dispersal: 0–5 m per generation time, wind dispersal: 2–500 m,
 631 animals as dispersal vector: 400–1500 m) (18, 27). Changing the global dispersal kernel scale
 632 parameter allows us to test the effect of a globally low to high ability of vegetation floras to
 633 respond to climatic changes by dispersal, while maintaining the skewed nature of dispersal
 634 events.

635 In addition to dispersal-based adaptation, at every time step, a flora's T_{opt} and A_{opt} traits evolve
 636 *in situ* towards local environmental conditions at a varying prescribed maximum adaptation rate
 637 (θ for temperature and α for aridity), representing adaptive evolutionary processes. Climatic
 638 niche adaptation is the result of multiple processes that are interdependent and that act on
 639 different spatiotemporal scales, ranging from phenotypic plasticity, to changes in species
 640 composition, to actual evolutionary innovation (60). The speed at which species and entire floras
 641 can adapt to new climatic conditions is associated with large uncertainty (19, 20, 26). We thus
 642 test a large range of flora climatic niche adaptation rates, ranging from very slow (highly
 643 conserved climatic niche) to near-immediate adaptation. For temperature adaptation, we vary θ
 644 from 0–10°C Ma⁻¹ between simulations, covering the empirical uncertainty range (19, 20, 26).
 645 Regarding aridity adaptation, we vary α from 0 to 100 Budyko units Ma⁻¹ with the upper end-
 646 member representing a vegetation response that is not limited by aridity.

647 After dispersal and adaptation, a competition scheme determines the best-adapted flora that will
 648 ultimately occupy a terrestrial grid cell. For this scheme, a performance function (Ω) captures
 649 the degree of adaptation of each flora in each grid cell, considering the deviation of a flora's
 650 T_{opt} and A_{opt} to local climatic conditions as follows:

$$\Omega = T_{adaptation} \cdot A_{adaptation} \quad (2)$$

$$T_{adaptation} = \exp\left(-\beta_T \cdot (T_{opt} - T_{local})^2\right) \quad (3)$$

$$A_{adaptation} = \exp\left(-\beta_A \cdot (A_{opt} - A_{local})^2\right) \quad (4)$$

651 where T_{local} and A_{local} are the grid cell's temperature and the local BAI, and β_T and β_A are the
 652 penalty parameters describing the performance of a flora for a given deviation of temperature
 653 and aridity from the flora's optimum (for the previously described niche width of approximately
 654 10°C and 2 BAI units, the parameters are fixed at 0.1 and 5 for temperature and aridity,
 655 respectively). In addition to flora extinction due to competition, floras are assumed to die out if
 656 the prevailing temperature differs from the temperature niche by more than 15°C or if the
 657 prevailing aridity differs by more than 5 BAI units from the flora's niche, to avoid unrealistically
 658 large climate niche deviations. When combined, the modelled eco-evolutionary processes
 659 depict the vegetation response to a climatic change and how it varies depending on the
 660 vegetation's dispersal and adaptive evolution capacity. To assess the sensitivity of the global
 661 post-LIP climate evolution to the vegetation's ability to respond and adapt, the coupled carbon-
 662 climate-vegetation model is run for over 12,000 combinations of θ , α and γ .

663 **Carbon cycling.** At every time step, a model of the geologic carbon cycle tracks the carbon
 664 exchange between geologic reservoirs and the atmosphere-ocean carbon pool, from which
 665 atmospheric CO₂ and climate conditions are derived. The mass balance of the surface system is:

$$\frac{M_{AO}}{dt} = F_{degassing} + F_{LIP} - F_{silw} - F_{locb} - F_{mocb} \quad (5)$$

666 where M_{AO} is the mass of carbon in the exogenic system, $F_{degassing}$ a background inorganic and
 667 organic carbon degassing rate, F_{LIP} the carbon injection due to LIP magmatic activity, F_{silw} the
 668 carbon burial due to silicate mineral weathering, F_{locb} the burial of terrestrially derived organic
 669 carbon, and F_{mocb} the burial of marine organic carbon.

670 Terrestrial organic carbon production is considered a function of a flora's state of adaptation to
 671 its local environment, as well as abiotic factors. A flora's net primary productivity (NPP) per
 672 time step is calculated as:

$$NPP = \epsilon^* \cdot RSS \cdot T_{lim} \cdot A_{lim} \cdot \Omega \quad (6)$$

673 ϵ^* is the radiation conversion efficiency, scaled to obtain a present-day land-derived organic
 674 carbon burial rate (F_{locb}) of about $3.5 \cdot 10^{12}$ mol C year⁻¹ (25) with present-day climate and
 675 geographic boundary conditions and assuming a constant burial efficiency b_{eff} (0.0007) of NPP
 676 [$F_{locb} = b_{eff} \cdot NPP$, with b_{eff} derived from present day rates of NPP and organic carbon
 677 burial (25, 64)]. RSS the surface net shortwave radiation. T_{lim} a temperature limitation factor

678 that is 0 for mean annual temperatures lower than -10°C or higher than 55°C , 1 for temperatures
 679 between 0 and 45°C , and linearly interpolated for transition temperatures. A_{lim} the water
 680 limitation of productivity, expressed as a function of the local BAI:

$$A_{lim} = 1 - \frac{1}{1 + \exp(-3 \cdot (BAI - 2))} \quad (7)$$

681 A_{lim} is approximately 1 in humid zones (BAI: 0–1.2), 0.5 at the transition from semi-humid to
 682 semi-arid (BAI: 2), and 0 for arid to hyperarid regions (BAI: 4–6). Ω again represents the flora's
 683 state of adaptation and performance in local conditions. A comparison of modelled NPP rates
 684 with this simplified vegetation model and data-based estimates for the present day is shown in
 685 fig. S10.

686 Marine primary productivity is approximated using an empirically derived chlorophyll-
 687 normalized temperature dependence of photosynthetic productivity P_b^{opt} (65) that accounts for
 688 temperature-limited productivity at sea surface temperatures (SST) below 20°C and nutrient- or
 689 stratification-limited productivity at temperatures higher than 20°C . Further, ocean productivity
 690 is taken to be proportional to silicate weathering rates, assuming that silicate weathering on land
 691 is the main nutrient input (i.e., phosphorus) to the ocean (66):

$$NPP_{ocean} = \phi_{scale} \cdot P_b^{opt}(SST) \cdot \frac{F_{silw}}{F_{silw,0}} \quad (8)$$

692 where ϕ_{scale} is a scaling factor used to obtain a present-day F_{mocb} of $3.5 \cdot 10^{12}$ mol C year $^{-1}$ (25),
 693 with present-day climatic and geographic boundary conditions and assuming a constant burial
 694 efficiency of NPP ($F_{mocb} = b_{eff} \cdot NPP_{ocean}$); F_{silw} the current time step's rate of continental
 695 silicate weathering; and $F_{silw,0}$ the initial rate of continental silicate weathering.

696 Following other deep-time biogeochemical models (66), silicate weathering is calculated using
 697 the approach by (67) where it is expressed as a function of local erosion, temperature and runoff:

$$\omega_{silw} = \chi_m \cdot \varepsilon \cdot \left(1 - \exp \left[-K \cdot e^{\frac{E_a}{RT_0} - \frac{E_a}{RT}} \cdot (1 - e^{-k_w \cdot q}) \cdot \frac{(z/\varepsilon)^{\sigma+1}}{(\sigma + 1)} \right] \right) \cdot f_{NPP} \quad (9)$$

698 where ω_{silw} is the flux of cations released during silicate weathering. ε is the local erosion,
 699 calculated as a function of topographic slope (s), runoff (q) and a scale parameter k_e (calibrated
 700 to reproduce present day rates of erosion) (68):

$$\varepsilon = k_e \cdot q^{0.5} \cdot s \quad (10)$$

701 In Eq. 9, T is the local temperature, χ_m the cation abundance in the bedrock (0.1), z the regolith
 702 thickness (10 m), E_a the apparent activation energy of silicate weathering (20 kJ mol^{-1}), R the

703 ideal gas constant and T_0 the standard temperature. K , k_w and σ are three calibration constants
 704 ($6 \cdot 10^{-5}$, $1 \cdot 10^{-3}$ and -0.1) [all adapted from (66)]. As in other geologic carbon cycle models,
 705 the weathering parameters are kept constant in all simulations due to the lack of detailed global
 706 lithologic information for the geologic past.

707 Finally, f_{NPP} in Eq. 9 is a weathering enhancement factor representing the local vegetation-
 708 mediated enhancement of mineral weathering as a function of the local flora's productivity and
 709 adaptation state. It is derived using a normalized vegetation productivity potential (NPP_{norm} ,
 710 between 0 and 1):

$$NPP_{norm} = \frac{RSS}{RSS_{max}} \cdot T_{lim} \cdot A_{lim} \cdot \Omega \quad (11)$$

711 where RSS_{max} is $5000 \text{ MJ m}^{-2} \text{ year}^{-1}$ (tropical radiation intensity), representing the threshold
 712 for non-radiation-limited photosynthesis.

713 Following (25), the vegetation-mediated enhancement is then calculated as:

$$f_{NPP} = \left[(1 - \min(NPP_{norm}, 1)) \cdot PREPLANT \cdot RCO_2^{0.5} + NPP_{norm} \right] \quad (12)$$

714 where RCO_2 the ratio of the current atmospheric CO_2 concentration to the initial concentration,
 715 and $PREPLANT$ is the weathering efficiency in the absence of plants. The choice of
 716 $PREPLANT$ defines the difference in weathering enhancement between bare ground and
 717 vegetated land. We test two values for the $PREPLANT$ parameter, $1/4$ (fig. 2) and $1/6$ (fig. S3),
 718 which correspond to a maximum four-fold and a six-fold increase in weathering rates in areas
 719 with high plant primary productivity. The considered vegetation-mediated weathering
 720 enhancement corresponds to the range observed in laboratory and field studies and to the values
 721 used in other deep-time biogeochemical models (9, 10, 12, 25).

722 The current timestep's rate of CO_2 consumption by silicate weathering is assumed to be
 723 proportional to the cation release ω_{silw} (66), with a present-day rate of carbon burial due to
 724 silicate weathering ($k_{silw,ref}$) of $1.0 \cdot 10^{13} \text{ mol C year}^{-1}$ (25) and a present-day cation release
 725 ($\omega_{silw,ref}$) calculated for the present-day topography and climate.

$$F_{silw} = k_{silw,ref} \cdot \frac{\omega_{silw}}{\omega_{silw,ref}} \quad (13)$$

726 The last carbon flux considered is the degassing of carbon from the solid Earth into Earth's
 727 atmosphere and ocean. $F_{degassing}$ denotes the background inorganic and organic carbon
 728 degassing from magmatism and volcanism. It is also assumed to include possible carbon
 729 contributions from oxidative weathering of organic carbon stored in rocks. Given that for a
 730 multi-million-year period, the geologic carbon cycle is assumed to be in a $\pm 5\%$ balance between

731 carbon source and sink fluxes (69, 70), $F_{degassing}$ is set equal to all carbon sink fluxes
 732 ($F_{degassing} = F_{silw} + F_{locb} + F_{mocb}$) at the start of a simulation. During the first 800 kyr of the
 733 model period, only small fluctuations in degassing are imposed, with the variations drawn
 734 randomly from a normal distribution with a mean of 0 and a standard deviation of $1 \cdot 10^{11}$ mol
 735 C year⁻¹. This background rate of degassing is being emitted to the atmosphere-ocean carbon
 736 pool throughout the simulations. During the LIP phase, F_{LIP} represents the estimated carbon
 737 injection due to LIP magmatism. The duration and mass of degassing is varied according to
 738 estimated degassing potentials of the Siberian Traps (Permian–Triassic), the Central Atlantic
 739 Magmatic Province (Triassic–Jurassic) and the North Atlantic Igneous Province (Paleocene–
 740 Eocene) (see main article).

741 We test the effect of seafloor weathering CO₂ consumption as an additional carbon cycle
 742 feedback. Seafloor weathering is approximated following (66) as a global flux dependent on the
 743 global average surface temperature:

$$F_{sfw} = k_{sfw,ref} \cdot e^{0.0608 \cdot (T_{GAST} - 288)} \quad (14)$$

744 where $k_{sfw,ref}$ is a reference weathering rate of $1.75 \cdot 10^{12}$ mol C year⁻¹ at a reference global
 745 average surface temperature of 288 K, and T_{GAST} is the current global average surface
 746 temperature. Additionally, we test the sensitivity of the results to a weaker CO₂-induced
 747 weathering enhancement in the absence of vegetation ($RCO_2^{0.3}$ instead of $RCO_2^{0.5}$ in Eq. 12).
 748 The results of these sensitivity tests are shown in fig. S11 for the Permian-Triassic
 749 paleogeographic configuration.

750 To obtain a first-order approximation of how the modelled changes in organic and inorganic
 751 carbon fluxes after a LIP degassing event affect the isotopic signature of buried carbonate
 752 carbon ($\delta^{13}C_{carb}$), we follow (71), assuming a steady state in the atmosphere-ocean $\delta^{13}C$ for a
 753 model time step larger than the residence time of carbon in the ocean ($\approx 10^5$ years):

$$\delta^{13}C_{in} = \delta^{13}C_{org} \cdot f_{org} + \delta^{13}C_{carb} \cdot (1 - f_{org}) \quad (15)$$

754 To derive the $\delta^{13}C$ of buried carbonate carbon, an average isotopic composition of degassed
 755 carbon $\delta^{13}C_{in}$ of -6‰ and an average isotopic composition of buried organic carbon $\delta^{13}C_{org}$
 756 of -27‰ are assumed. Finally, f_{org} defines the ratio of total organic (marine + terrestrial) to
 757 total organic and inorganic (from silicate + carbonate weathering) carbon burial. While
 758 carbonate weathering affects the $\delta^{13}C$ balance, it is a CO₂-neutral process for long time scales
 759 (72) and therefore is not included in the atmosphere-ocean carbon balance. It is approximated
 760 following (66) and calculated based on spatial fields of runoff and biotic weathering
 761 enhancement as:

$$F_{carb\omega} = k_{carb\omega} \cdot q \cdot f_{NPP} \quad (16)$$

762 where $k_{carb\omega}$ represents a scale parameter, included to obtain a present-day rate of carbonate
 763 weathering of $8 \cdot 10^{12}$ mol C year⁻¹ with present-day topography and climate conditions (66). A
 764 comparison of modelled and observed carbonate $\delta^{13}C$ for the Permian-Triassic and the
 765 Paleocene-Eocene is shown in fig. S4.

766 **Climate model.** With the carbon cycle model, carbon fluxes in and out of the combined pool of
 767 Earth's atmosphere and oceans are tracked. Assuming a baseline atmosphere-ocean carbon mass
 768 M_{AO} of $3.193 \cdot 10^{18}$ mol C at a 280 ppm atmospheric CO₂ concentration (25), atmospheric CO₂
 769 concentration is set to be proportional to the square of the total carbon in the atmosphere-ocean
 770 pool (73):

$$CO_{2,t} = CO_{2,0} \cdot \left(\frac{M_{AO,t}}{M_{AO,0}} \right)^2 \quad (17)$$

771 where $CO_{2,t}$ is the current and $CO_{2,0}$ the initial CO₂ concentration; $M_{AO,t}$ the current and $M_{AO,0}$
 772 the initial atmosphere-ocean carbon content, respectively.

773 A full dynamic coupling of a climate model with the above-described vegetation and carbon
 774 cycle model is currently not feasible, first because of computational limitations (climate models
 775 integrate over periods of hundreds to several thousand years, not the multi-million-year periods
 776 considered here), and second, because standard vegetation models integrated into climate
 777 models do not include the eco-evolutionary dynamics considered here (i.e., dispersal and
 778 adaptation processes). To overcome this limitation, we follow an approach commonly used in
 779 geologic carbon cycle modelling (66, 74), where climatic conditions at every model time step
 780 are interpolated from a lookup table of pre-run climate simulations. A quantification of the
 781 uncertainty in surface climatic conditions arising from implementing this interpolation routine
 782 instead of running a new climate model for each time step's atmospheric CO₂ concentration is
 783 illustrated in fig. S12. To create the climate lookup table, an Earth system model of intermediate
 784 complexity, PlaSim (75, 76), is run for atmospheric CO₂ concentrations between 100 and 8000
 785 ppm for each considered continental configuration (from 100 to 1000 ppm in 50 ppm steps,
 786 from 1125 to 3000 in 125 ppm steps, and from 3000 to 8000 in 500 ppm steps). For each studied
 787 period, the solar luminosity is adjusted following the solar physics model of Gough (77). PlaSim
 788 is run with a mixed-layer slab ocean model and thermodynamic sea ice. To avoid confounding
 789 effects with vegetation models that can be coupled to PlaSim, the climate model is run without
 790 dynamic vegetation, with a uniform surface albedo on land (0.2), and with a constant soil depth
 791 (0.15 m). For each atmospheric CO₂ concentration, PlaSim is run for 250 model years, using the
 792 average temperature, precipitation, runoff and radiation of the last 50 model years to inform the

793 eco-evolutionary vegetation model and the carbon cycle processes explained above. The
794 continental configurations for the PlaSim simulations, as well as the other model components,
795 are taken from (54) (maps for Permian-Triassic, Triassic-Jurassic and present) and from (55)
796 for the Paleocene-Eocene and are assumed to be fixed for the entire 8 Ma model period. It should
797 be noted that, as we do not fully integrate the studied vegetation dynamics into the PlaSim
798 climate model, we can only consider the effects of eco-evolutionary vegetation on climate
799 through changes in the atmosphere-ocean carbon content, and not through direct interactions
800 with the climate system, including changes to surface albedo, water and energy exchange.

801 Paleotemperature proxies

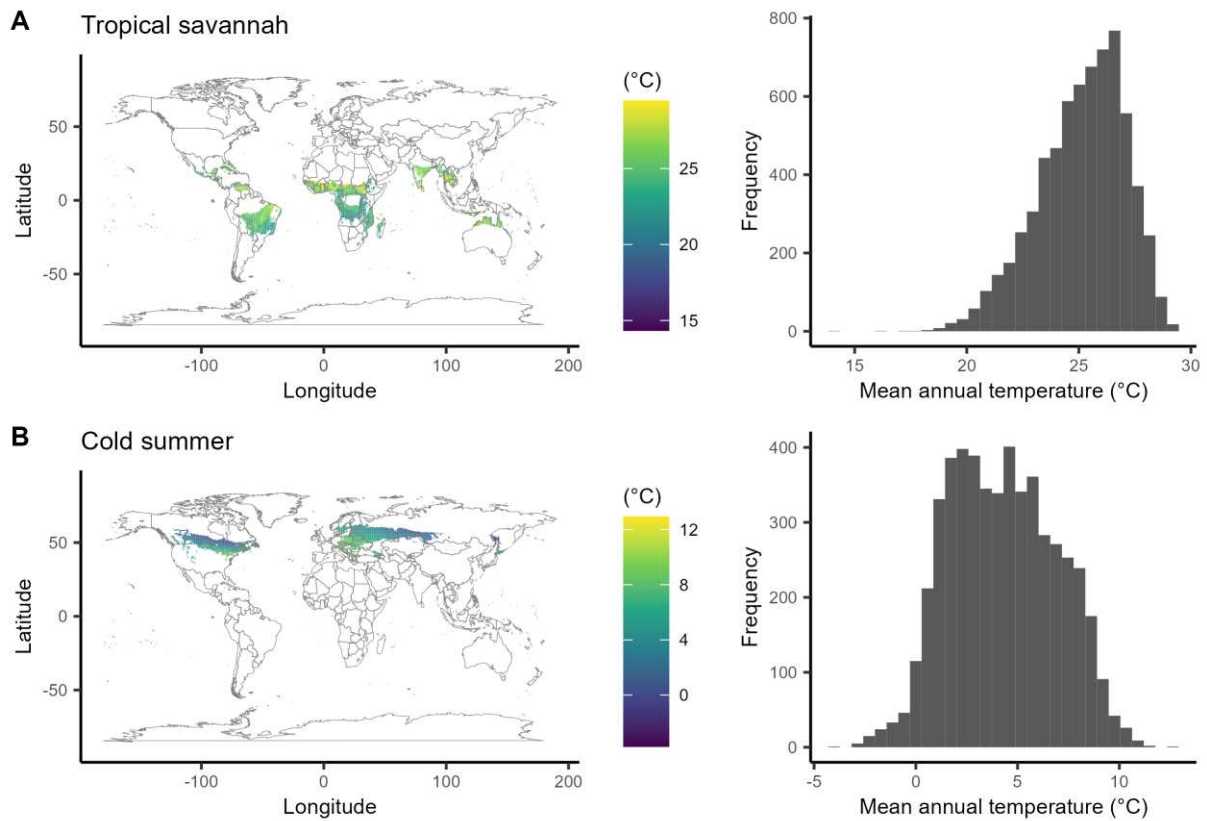
802 The records documenting the sea surface temperature changes ($\Delta SST_{composite}$) across the
803 Permian–Triassic, Triassic–Jurassic, and Paleocene–Eocene boundaries (Fig. 2) are compiled
804 using proxy data from the PhanSST database (53). For each time slice, we utilize data from the
805 chronostratigraphic stage (i.e., geochronologic age) preceding the LIP-associated boundary and
806 the two to three stages postdating the boundary. The Ypresian (Eocene) is subdivided into three
807 equal time bins (sub-stages) due to its extended duration, high data density, and reliable age
808 control (53), and the PETM data are further subdivided following (32).

809 For each of the three boundaries, we isolate records from the same site and proxy system that
810 have unaltered data from at least two of the (sub-)stages, following the diagenetic screening
811 protocol of (53). This results in 15 unique records for the Permian–Triassic transition (14
812 $\delta^{18}O_{phosphate}$ and one $\delta^{18}O_{carbonate}$), 11 records for the Triassic–Jurassic (10 $\delta^{18}O_{carbonate}$, 1
813 TEX_{86}), and 36 records for the PETM (11 $\delta^{18}O_{carbonate}$, 14 TEX_{86} , and 11 Mg/Ca). Sample
814 sites for each period are shown in fig. S13.

815 Sea surface temperatures (SSTs) are estimated from the proxy data using established transfer
816 functions or proxy system models (78–84). Conodont $\delta^{18}O_{phosphate}$ data are brought into the
817 same reference frame using an NBS-120c standard value of 21.7‰ and a Durango standard
818 value of 9.8‰. Both BAYFOX (82) and BAYSPAR (83) are run using a prior mean value of
819 25°C and a prior standard deviation of 10°C. BAYMAG is run using a prior standard deviation
820 of 10°C, the newest version of the seawater Mg/Ca curve (i.e., option 2 in BAYMAG), an H
821 value of 0.75 (84), and an omega value of 5. With both BAYFOX and BAYMAG, we use the
822 pooled species annual calibration. Estimating absolute SST from oxygen isotope data requires
823 an assumption about the $\delta^{18}O$ value of the seawater (78–82), which is difficult to constrain in
824 deep time. However, this assumption is negated when calculating SST differences between time
825 intervals, provided that the seawater composition remained constant across any given record.

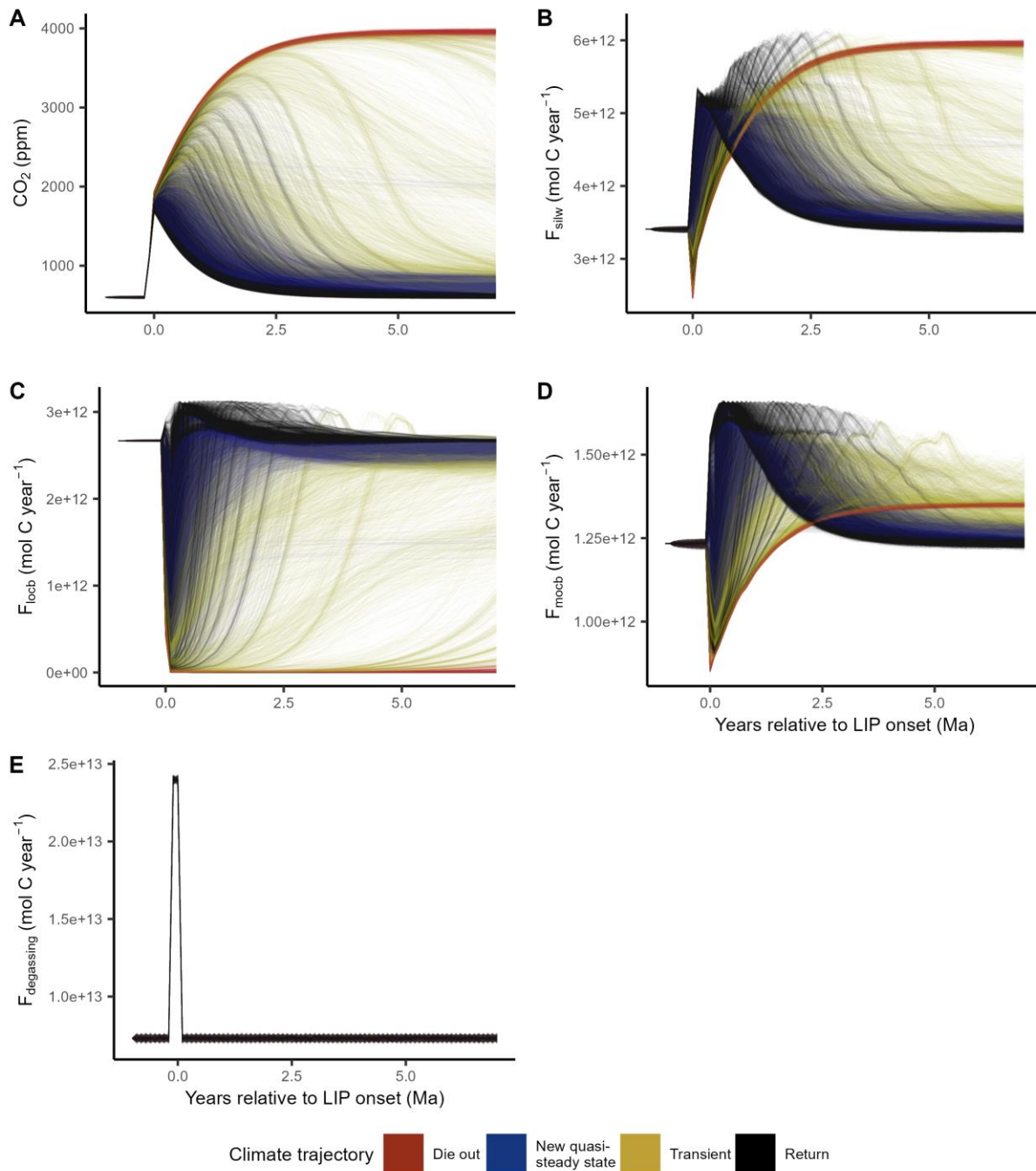
826 $\Delta SST_{composite}$ is estimated by subtracting the median pre-LIP SST of each record from each data
827 point in that record. Not all records have data from the stage preceding the LIP-associated

828 transition; in those instances, we use the median Δ SST of the subsequent (sub-)stage from the
829 records with pre-LIP data to estimate a baseline Δ SST for each remaining record.



830
831
832
833
834
835
836

Fig. S1: Range of mean annual temperatures observed within Koeppen-Geiger vegetation zones. Location and temperature range within the **A.** tropical savannah and **B.** cold summer Koeppen-Geiger zone. Koeppen-Geiger zones are often used to distinguish among contrasting biological and climatic regions on Earth that are characterized by similar vegetation types. The range of mean annual temperatures observed within a Koeppen-Geiger zone is approximately 10°C, which is the temperature niche width used for the modelled floras. Data from (61).



837

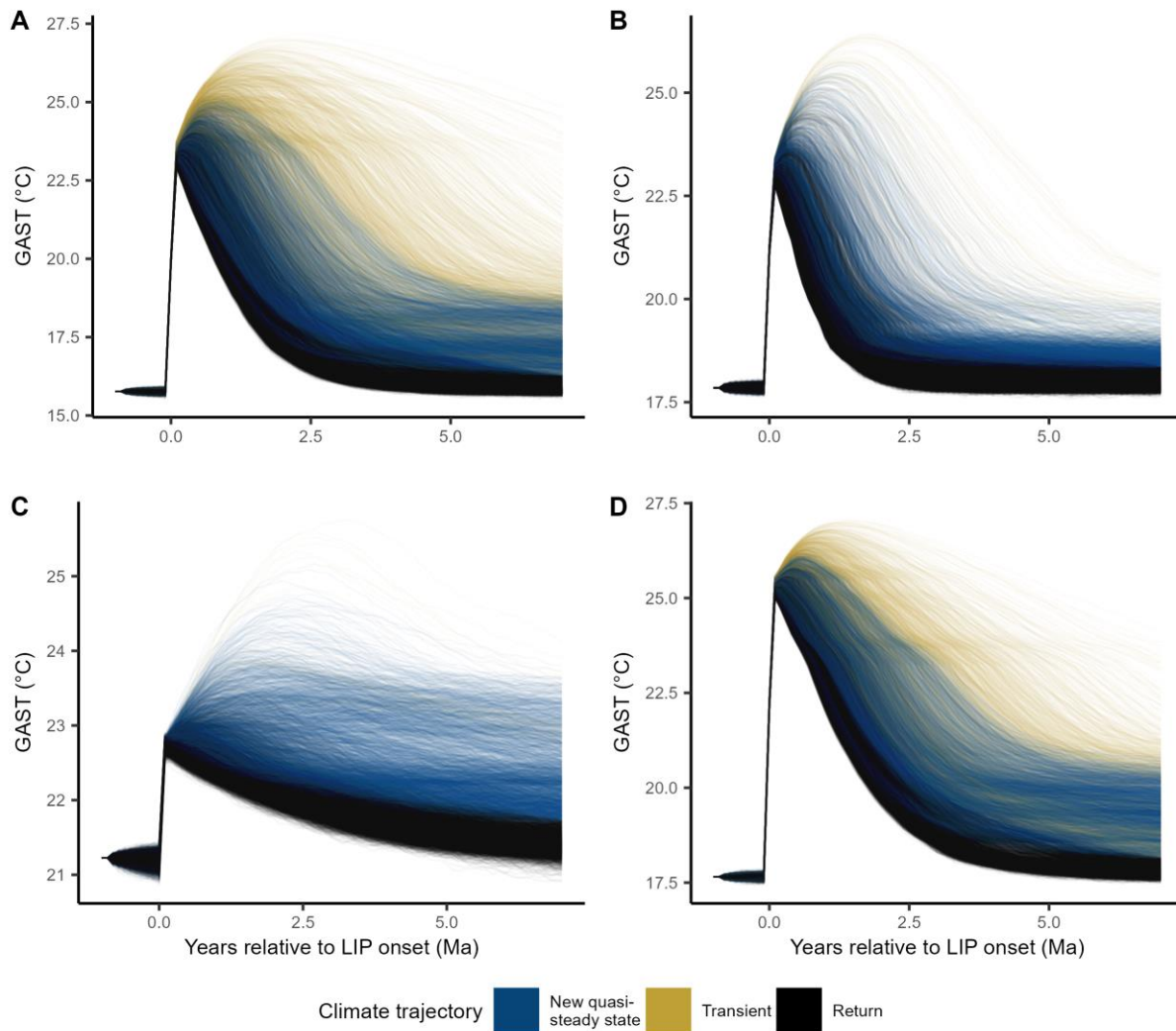
838

839

840

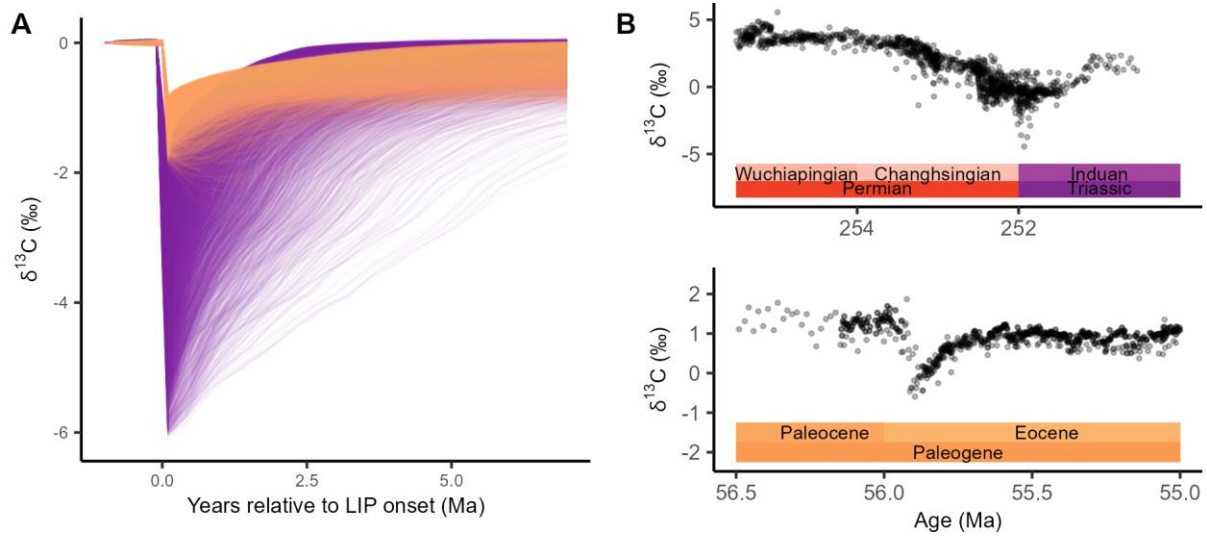
841

Fig. S2: Carbon flux dynamics for modelled range of climate trajectories observed for the Siberian Traps Large Igneous Province (Permian–Triassic transition). **A.** atmospheric CO₂ concentration, **B.** silicate weathering (F_{silw}), **C.** land-derived organic carbon burial (F_{locb}), **D.** marine organic carbon burial (F_{mocb}), **E.** carbon degassing (background + LIP) ($F_{degassing}$).



842
843
844
845
846
847
848
849
850

Fig. S3: Global average temperature (GAST) trajectories for an alternative set of model boundary conditions. **A.** Permian-Triassic configuration with an increased sensitivity of silicate weathering to plant primary productivity: maximum six-fold increase in weathering rates in highly productive areas compared with four-fold in the default configuration. **B.** Triassic-Jurassic configuration with an increased sensitivity of silicate weathering to plant primary productivity (maximum six-fold enhancement). **C.** Paleocene-Eocene configuration with a reduced carbon degassing mass of 8'000 Gt (instead of 15'000 in main the main text). **D.** Permian-Triassic configuration with a higher starting CO₂ concentration of 800 ppm (instead of 600 ppm in the main text) and a greater mass of carbon degassing of 50,000 Gt (instead of 40,000 Gt in the main text).



851

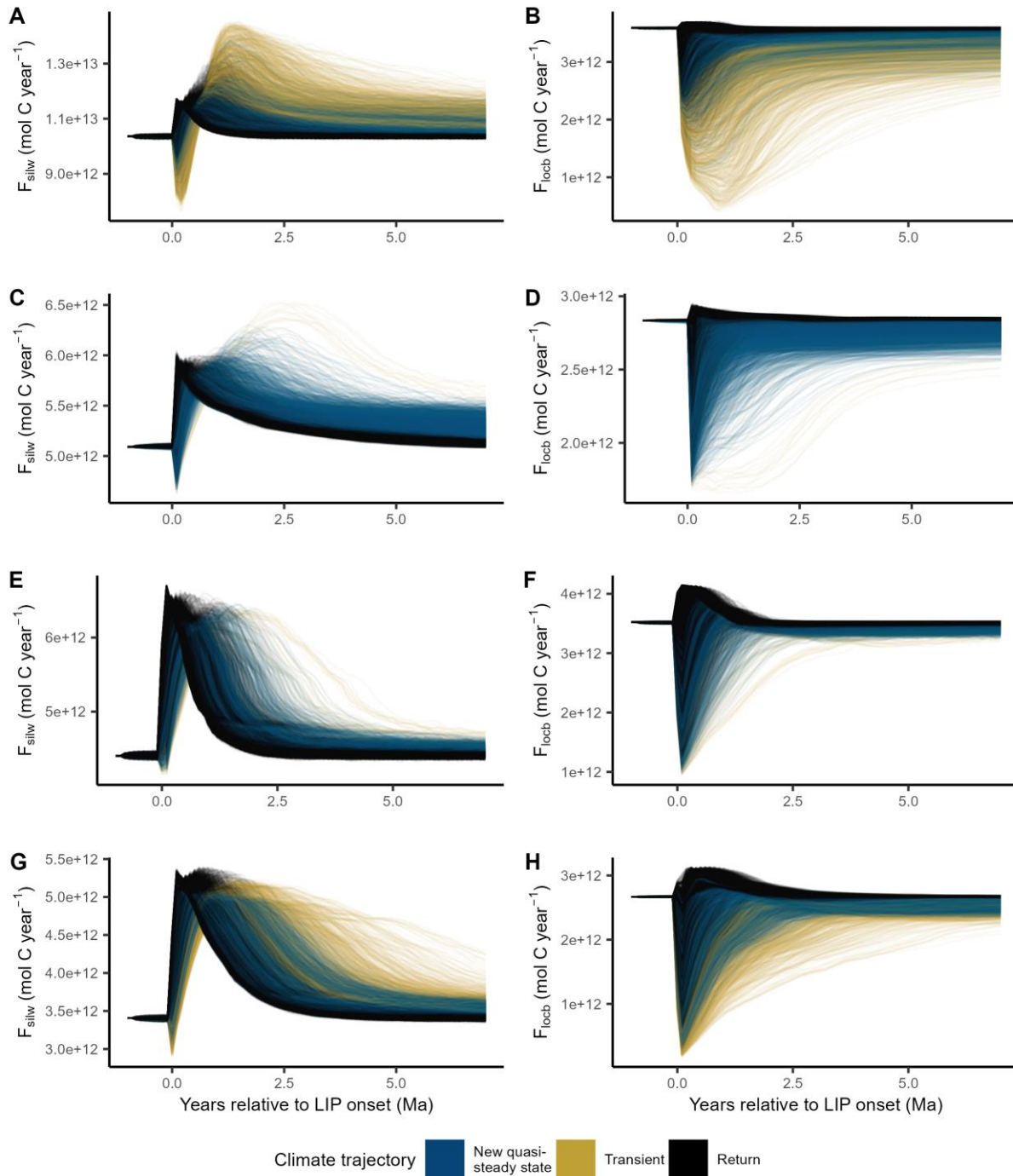
852

853

854

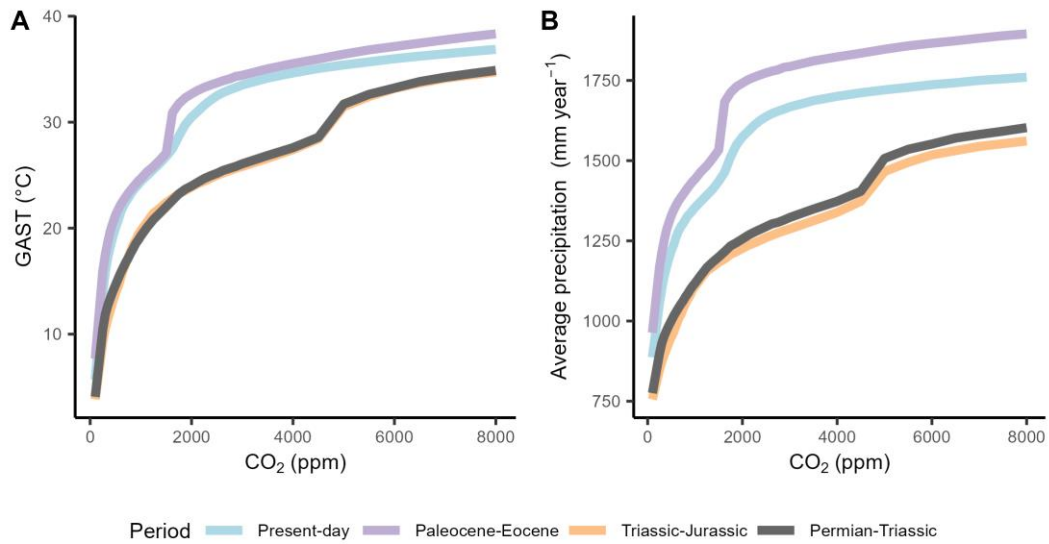
855

Fig. S4: Post-Large Igneous Province carbonate $\delta^{13}\text{C}$ dynamics. **A.** Modelled changes in the carbonate $\delta^{13}\text{C}$ record based on changes in organic and inorganic carbon burial. **B.** composite $\delta^{13}\text{C}$ curve over the Permian–Triassic boundary from various sources, as compiled in (85) (only Iran sections shown), and benthic $\delta^{13}\text{C}$ data over the Paleocene–Eocene boundary from ODP sites 1209, 1262 and 1263 from various sources, as compiled in (86, 87).



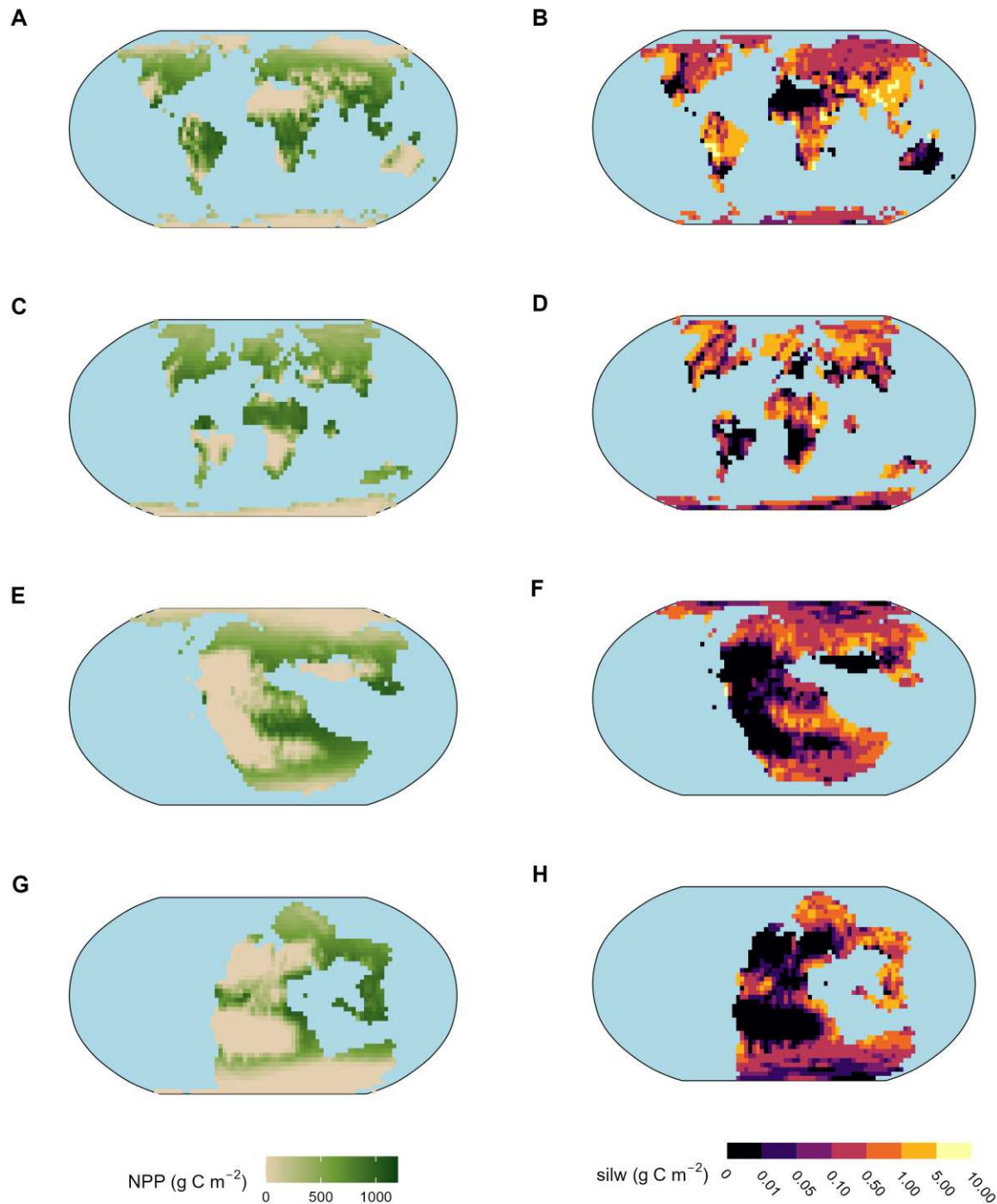
856
857
858
859
860

Fig. S5: Carbon burial fluxes for the modelled Phanerozoic Large Igneous Province (LIP) degassing events. Silicate weathering (F_{silw} ; left column) and land-derived organic carbon burial (F_{locb} ; right column) for the present-day hypothetical LIP (A. & B.), the North Atlantic Igneous Province (Paleocene-Eocene) (C. & D.), the Central Atlantic Igneous Province (Triassic-Jurassic) (E. & F.), and the Siberian Traps (Permian-Triassic) (G. & H.).



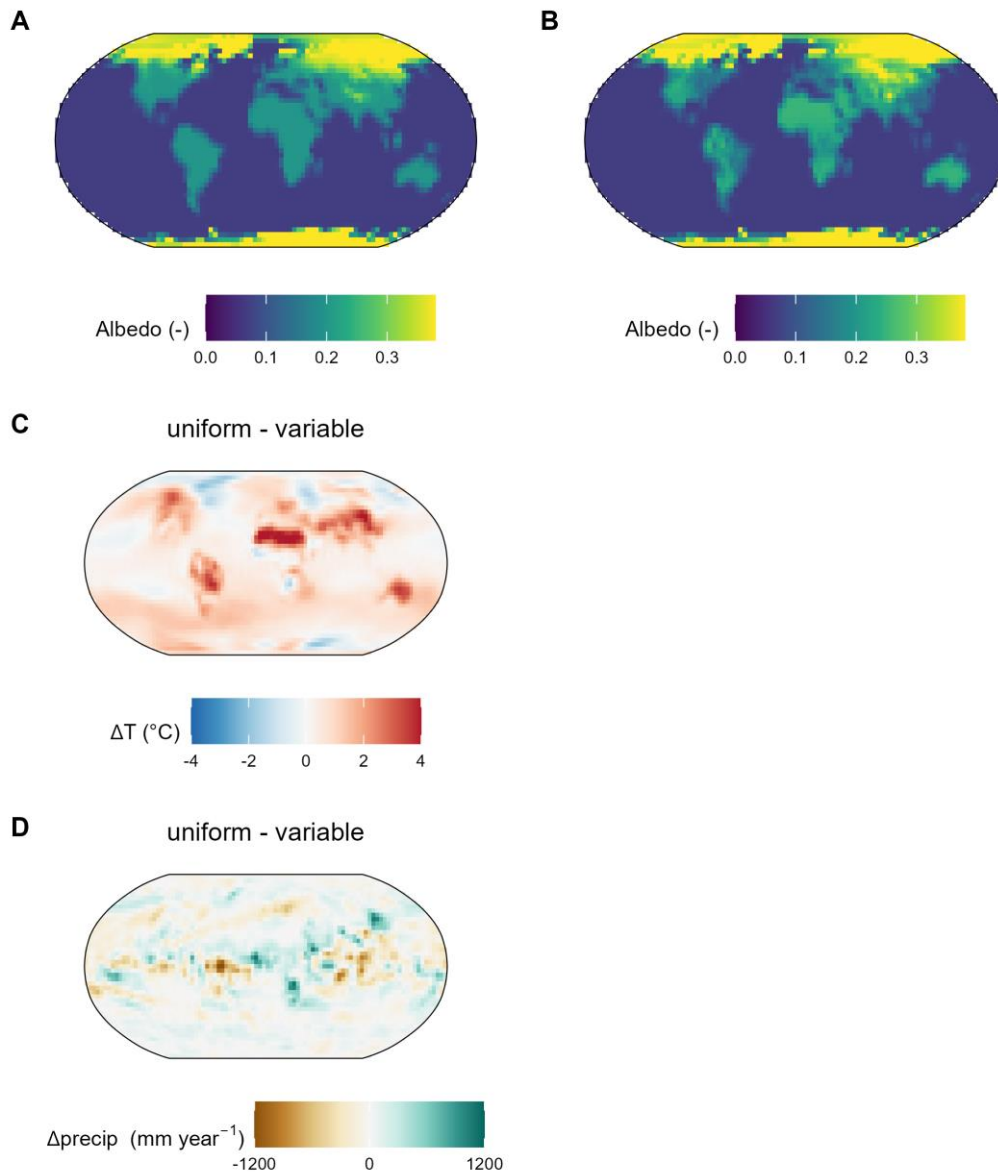
861
862
863
864
865

Fig. S6: Modelled climate sensitivity. **A.** Sensitivity of global average surface temperature (GAST) and **B.** global average precipitation to an increase in atmospheric CO₂ concentration as observed in the PlaSim climate simulations for the Permian-Triassic, Triassic-Jurassic, Paleocene-Eocene and present-day continental configurations.



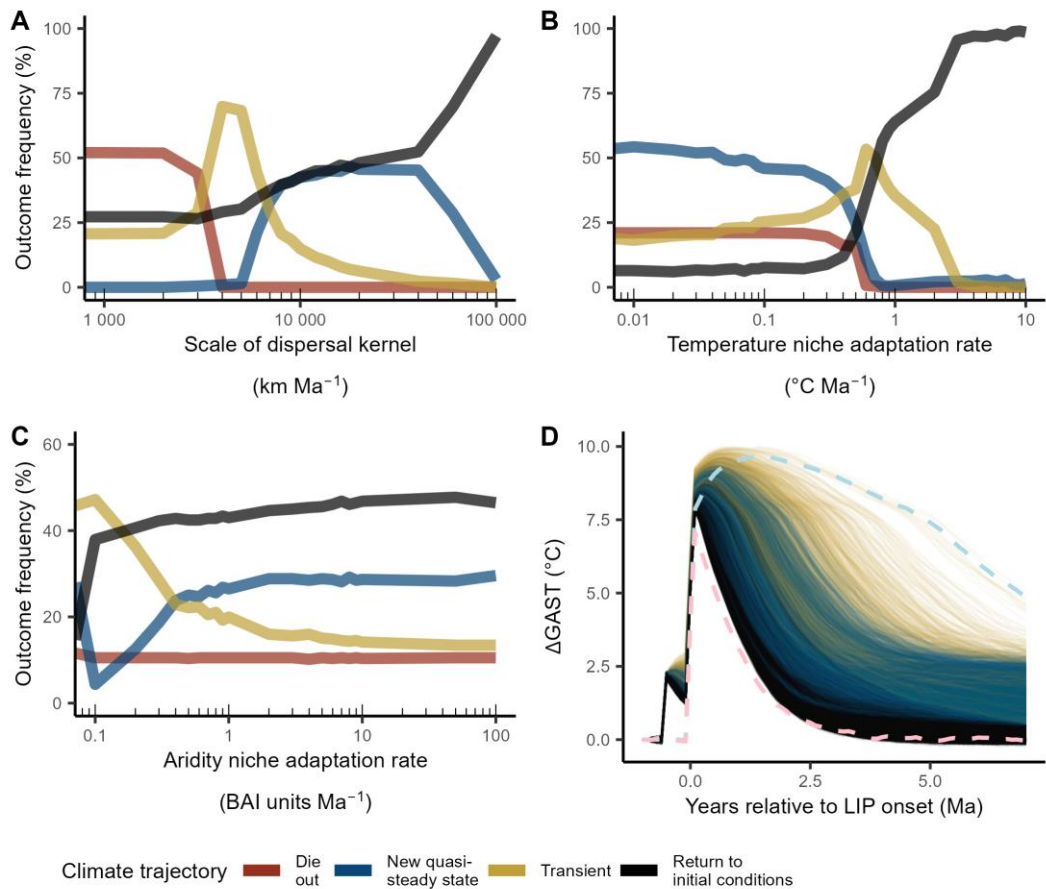
866
867
868
869
870
871
872

Fig. S7: Spatial distribution of net primary productivity (NPP) and silicate weathering carbon consumption. NPP (left column) and silicate weathering (silw; right column) for the present-day continental configuration (A. & B.), for the Paleocene-Eocene continental configuration (C. & D.), for the Triassic-Jurassic continental configuration (E. & F.), and for the Permian-Triassic continental configuration (G. & H.). Paleogeographic reconstructions are from (55) for the Paleocene-Eocene and otherwise from (54). Note that in the model, only a small fraction of NPP ultimately becomes buried (F_{loch}). Note also the uneven color scale for silicate weathering.



873
874
875
876
877
878
879
880

Fig. S8: Surface albedo-induced climate change. **A.** Uniform surface albedo of 0.2 on snow- and ice-free land. **B.** Example PlaSim climate simulation with an altered surface albedo scheme: higher surface background albedo of 0.25 and lower albedo only in areas with a potentially high vegetation cover as estimated by the PlaSim model. **C.** Difference in surface temperature between uniform and variable albedo scheme. If LIP-triggered vegetation shifts result in the exposure of surfaces of higher or lower albedo, a cooling or a warming effect on regional and global climate can be expected, respectively. **D.** Difference in annual precipitation between uniform and variable albedo scheme.



881

882

883

884

885

886

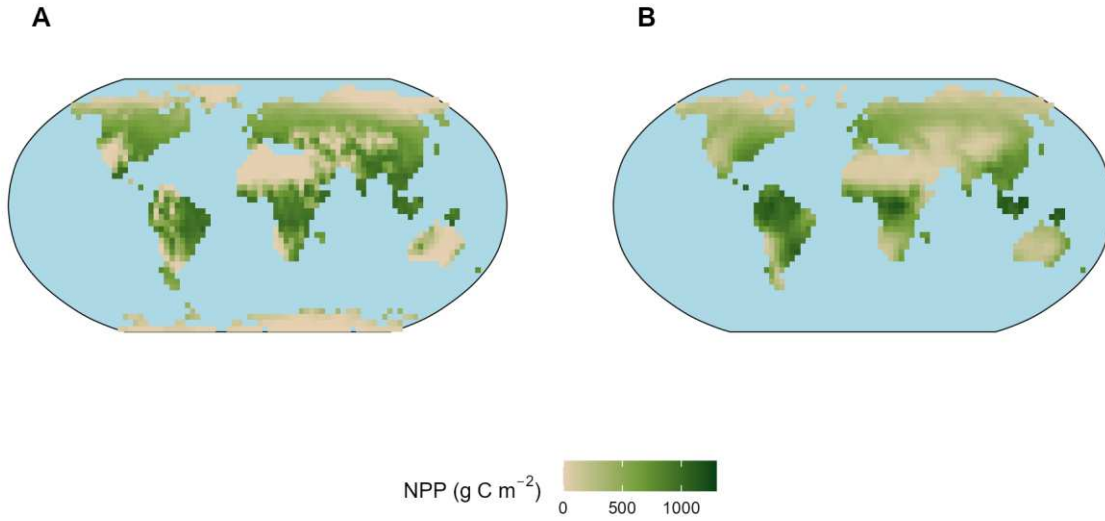
887

888

889

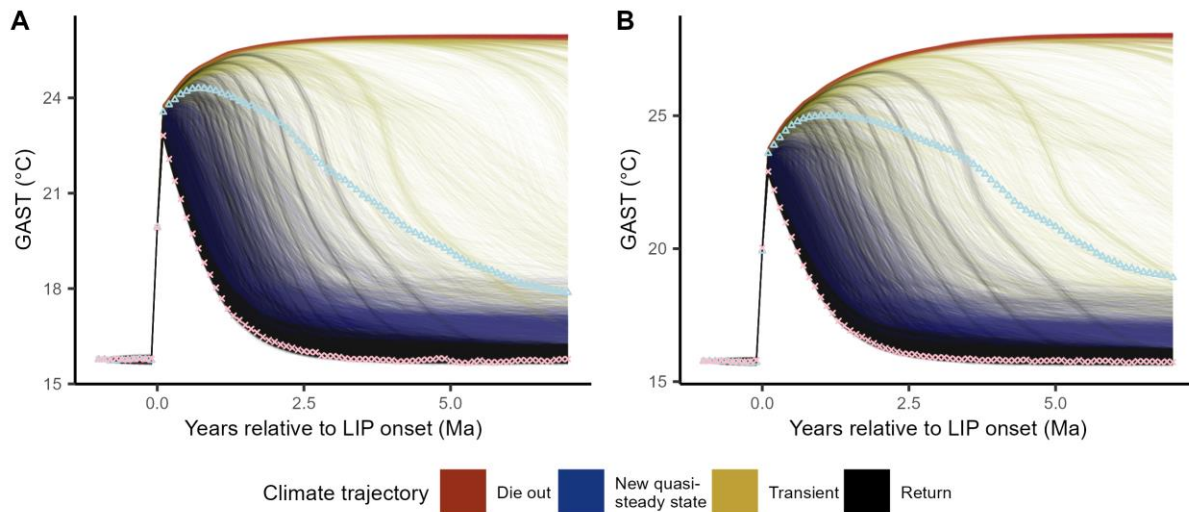
890

Fig. S9: Model results for pre-perturbed vegetation at onset of Large Igneous Province (LIP) degassing. This is achieved by imposing a carbon cycle perturbation before the onset of the LIP, resulting in non-optimally-adapted vegetation floras. Classification of the model outcome depending on **A.** the vegetation's dispersal capacity, **B.** the temperature niche adaptation rate, and **C.** the aridity niche adaptation rate. Model outcome frequencies are similar to the results presented in the main text, but with slightly more 'transient' trajectories that did not reach a steady state at the end of the simulation. **D.** Range of climate trajectories for a reduced biological parameter set (excluding 'die-out' trajectories and assuming non-zero temperature and aridity niche adaptation rates). For reference, the fast (pink) and slow (blue) vegetation adaptation end-member trajectories of the model presented in the main text are displayed.



891
892
893
894
895
896
897

Fig. S10: Validation of modelled net primary productivity (NPP). **A.** NPP modelled using the developed deep-time vegetation model and climate input data from the intermediate-complexity climate model PlaSim (CO_2 concentration of 400 ppm, resolution $3.75^\circ \times 3.75^\circ$; averaged over 50 model years) and topographic data from (54). **B.** NPP estimate by (64) using monthly average climate data from 1931 to 1961 (ensemble mean of 17 estimates derived from vegetation models and satellite data; resampled to the resolution of the eco-evolutionary vegetation model for comparison).



898

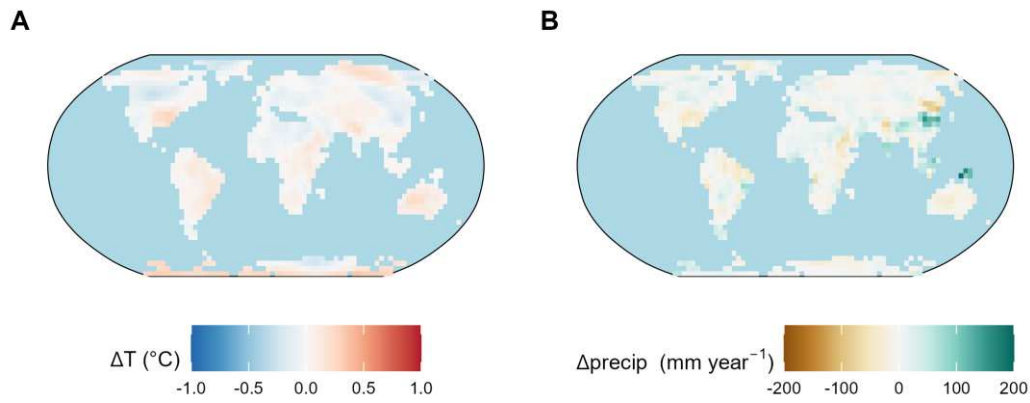
899

900

901

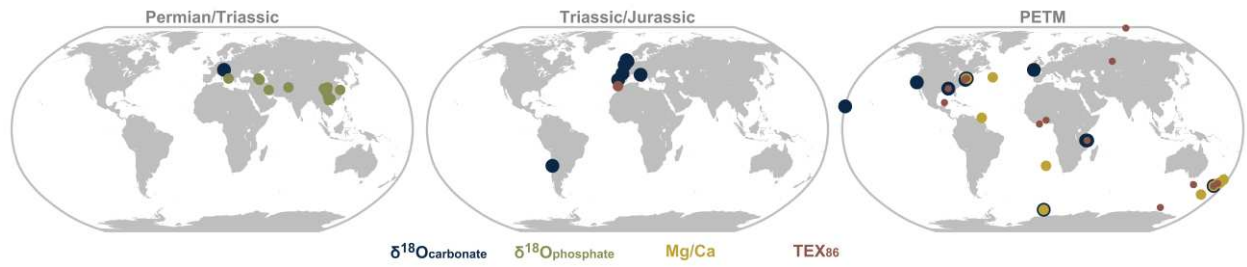
902

Fig. S11: Sensitivity of global average surface temperature trajectories (GAST) to carbon cycle feedback mechanisms. A. Permian-Triassic simulation with seafloor weathering feedback. **B.** Permian-Triassic simulation with seafloor weathering feedback but a weaker CO_2 -dependent weathering feedback in the absence of plants or in locations of reduced primary productivity ($RCO_2^{0.3}$ instead of $RCO_2^{0.5}$ in Eq. 12).



903
904
905
906

Fig. S12: Uncertainty in surface climatic conditions due to the climate interpolation routine. Plots depict the difference in **A.** surface temperature and **B.** precipitation between an interpolated climate for 800 ppm (interpolated from climate runs for 850 and 750 ppm) and an actual climate model output for 800 ppm.



907
908
909

Fig. S13: Sampling sites of paleotemperature proxies. Locations of analyzed proxies for **A.** the Permian–Triassic transition **B.** the Triassic–Jurassic transition, and **C.** the Paleocene–Eocene transition.

910
911
912
913
914
915
916
917
918
919
920
921
922
923
924
925
926
927
928
929
930
931
932
933
934
935
936
937
938
939
940
941
942
943
944

References

58. O. Hagen *et al.*, gen3sis: A general engine for eco-evolutionary simulations of the processes that shape Earth's biodiversity. *PLOS Biology* **19**, e3001340, DOI 10.1371/journal.pbio.3001340 (2021).
59. M. Huang *et al.*, Air temperature optima of vegetation productivity across global biomes. *Nature Ecology & Evolution* **3**, 772–779, DOI 10.1038/s41559-019-0838-x (2019).
60. M. J. Donoghue, E. J. Edwards, Biome shifts and niche evolution in plants. *Annual Review of Ecology, Evolution, and Systematics* **45**, 547–572, DOI 10.1146/annurev-ecolsys-120213091905 (2014).
61. H. E. Beck *et al.*, Present and future Koppen-Geiger climate classification maps at 1-km resolution. *Scientific Data* **5**, 180214, DOI 10.1038/sdata.2018.214 (2018).
62. A. Takeshima *et al.*, Global aridity changes due to differences in surface energy and water balance between 1.5°C and 2°C warming. *Environmental Research Letters* **15**, 0940a7, DOI 10.1088/1748-9326/ab9db3 (2020).
63. J. M. J. Travis *et al.*, Modelling dispersal: an eco-evolutionary framework incorporating emigration, movement, settlement behaviour and the multiple costs involved. *Methods in Ecology and Evolution* **3**, 628–641, DOI 10.1111/j.2041-210X.2012.00193.x (2012).
64. W. Cramer *et al.*, Comparing global models of terrestrial net primary productivity (NPP): overview and key results. *Global Change Biology* **5**, 1–15, DOI 10.1046/j.1365-2486.1999.00009.x (1999).
65. M. J. Behrenfeld, P. G. Falkowski, Photosynthetic rates derived from satellite-based chlorophyll concentration. *Limnology and Oceanography* **42**, 1–20, DOI 10.4319/lo.1997.42.1.0001 (1997).
66. B. J. Mills, Y. Donnadieu, Y. Godderis, Spatial continuous integration of Phanerozoic global biogeochemistry and climate. *Gondwana Research* **100**, 73–86, DOI 10.1016/j.gr.2021.02.011 (2021).
67. A. J. West, Thickness of the chemical weathering zone and implications for erosional and climatic drivers of weathering and for carbon-cycle feedbacks. *Geology* **40**, 811–814, DOI 10.1130/G33041.1 (2012).
68. P. Maffre *et al.*, Mountain ranges, climate and weathering. Do orogens strengthen or weaken the silicate weathering carbon sink? *Earth and Planetary Science Letters* **493**, 174–185, DOI 10.1016/j.epsl.2018.04.034 (2018).
69. R. A. Berner, K. Caldeira, The need for mass balance and feedback in the geochemical carbon cycle. *Geology* **25**, 955–956, DOI 10.1130/0091-7613(1997)025<0955:TNFMB>2.3.CO;2 (1997).

- 945 70. J. K. Caves, A. B. Jost, K. V. Lau, K. Maher, Cenozoic carbon cycle imbalances and a
946 variable weathering feedback. *Earth and Planetary Science Letters* **450**, 152–163, DOI
947 10.1016/j.epsl.2016.06.035 (2016).
- 948 71. G. A. Shields, B. J. W. Mills, Tectonic controls on the long-term carbon isotope mass
949 balance.
950 *Proceedings of the National Academy of Sciences of the United States of America* **114**,
951 4318–43232, DOI 10.1073/pnas.1614506114 (2017).
- 952 72. R. Berner, A model for atmospheric CO₂ over Phanerozoic time. *American Journal of*
953 *Science* **291**, 339–376, DOI 10.2475/ajs.291.4.339 (1991).
- 954 73. L. R. Kump, M. A. Arthur, Interpreting carbon-isotope excursions: carbonates and organic
955 matter. *Chemical Geology* **161**, 181–198, DOI 10.1016/S0009-2541(99)00086-8 (1999).
- 956 74. Y. Donnadieu *et al.*, A GEOCLIM simulation of climatic and biogeochemical
957 consequences of Pangea breakup. *Geochemistry, Geophysics, Geosystems* **7**, Q11019,
958 DOI 10.1029/2006GC001278 (2006).
- 959 75. K. Fraedrich, A suite of user-friendly global climate models: Hysteresis experiments. *The*
960 *European Physical Journal Plus* **127**, 53, DOI 10.1140/epjp/i2012-12053-7 (2012).
- 961 76. O. Mehling, K. Bellomo, M. Angeloni, C. Pasquero, J. Von Hardenberg, High-latitude
962 precipitation as a driver of multicentennial variability of the AMOC in a climate model of
963 intermediate complexity. *Climate Dynamics* **61**, 1519–1534, DOI 10.1007/s00382-022-
964 06640-3 (2023).
- 965 77. D. O. Gough, Solar interior structure and luminosity variations. *Solar Physics* **74**, 21–34
966 (1981).
- 967 78. E. Pucéat *et al.*, Revised phosphate–water fractionation equation reassessing
968 paleotemperatures derived from biogenic apatite. *Earth and Planetary Science Letters*
969 **298**, 135–142, DOI 10.1016/j.epsl.2010.07.034 (2010).
- 970 79. S.-T. Kim, J. R. O’Neil, Equilibrium and nonequilibrium oxygen isotope effects in
971 synthetic carbonates. *Geochimica et Cosmochimica Acta* **61**, 3461–3475, DOI
972 10.1016/S0016-7037(97)00169-5 (1997).
- 973 80. M. Daëron *et al.*, Most Earth-surface calcites precipitate out of isotopic equilibrium.
974 *Nature Communications* **10**, 429, DOI 10.1038/s41467-019-08336-5 (2019).
- 975 81. L. Grossman, T.-L. Ku, Oxygen and carbon isotope fractionation in biogenic aragonite:
976 temperature effects. *Chemical Geology* **59**, 59–74 (1986).
- 977 82. S. B. Malevich, L. Vetter, J. E. Tierney, Global core top calibration of ¹⁸O in planktic
978 foraminifera to sea surface temperature. *Paleoceanography and Paleoclimatology* **34**,
979 1292–1315, DOI 10.1029/2019PA003576 (2019).

- 980 83. J. E. Tierney, M. P. Tingley, A Bayesian, spatially-varying calibration model for the
981 TEX₈₆ proxy. *Geochimica et Cosmochimica Acta* **127**, 83–106, DOI
982 10.1016/j.gca.2013.11.026 (2014).
- 983 84. J. E. Tierney, S. B. Malevich, W. Gray, L. Vetter, K. Thirumalai, Bayesian calibration of
984 the Mg/Ca paleothermometer in planktic foraminifera. *Paleoceanography and*
985 *Paleoclimatology* **34**, 2005–2030, DOI 10.1029/2019PA003744 (2019).
- 986 85. M. Schobben *et al.*, Latest Permian carbonate carbon isotope variability traces
987 heterogeneous organic carbon accumulation and authigenic carbonate formation. *Climate*
988 *of the Past* **13**, 1635–1659, DOI 10.5194/cp-13-1635-2017 (2017).
- 989 86. T. Westerhold *et al.*, Astronomical calibration of the Ypresian timescale: implications for
990 seafloor spreading rates and the chaotic behavior of the solar system? *Climate of the Past*
991 **13**, 1129–1152, DOI 10.5194/cp-13-1129-2017 (2017).
- 992 87. T. Westerhold, U. Rohl, B. Donner, J. C. Zachos, Global extent of early Eocene
993 hyperthermal events: A new Pacific benthic foraminiferal isotope record from Shatsky
994 Rise (ODP Site 1209). *Paleoceanography and Paleoclimatology* **33**, 626–642, DOI
995 10.1029/2017PA003306 (2018).